Geomorphology 420 (2023) 108501

Contents lists available at ScienceDirect

Geomorphology

journal homepage: www.journals.elsevier.com/geomorphology

Landforms and degradation pattern of the Batagay thaw slump, Northeastern Siberia

Alexander I. Kizyakov [a,*], Sebastian Wetterich [b,1], Frank Günther [c], Thomas Opel [d], Loeka L. Jongejans [b,h], Jérémy Courtin [d], Hanno Meyer [d], Andrei G. Shepelev [e], Igor I. Syromyatnikov [f], Alexander N. Fedorov [e], Mikhail V. Zimin [g], Guido Grosse [b,h]

[a] Lomonosov Moscow State University, Cryolithology and Glaciology Department, Faculty of Geography, 119991 Moscow, Russia
[b] Alfred Wegener Institute Helmholtz Center for Polar and Marine Research, Permafrost Research Section, 14473 Potsdam, Germany
[c] Hochschule Neubrandenburg, Department of Landscape Sciences and Geomatics, 17033 Neubrandenburg, Germany
[d] Alfred Wegener Institute Helmholtz Center for Polar and Marine Research, Polar Terrestrial Environmental Systems Section, 14473 Potsdam, Germany
[e] Melnikov Permafrost Institute SB RAS, Laboratory of Permafrost Landscapes, 677010 Yakutsk, Russia
[f] Melnikov Permafrost Institute SB RAS, Laboratory of General Geocryology, 677010 Yakutsk, Russia
[g] Lomonosov Moscow State University, Department of Cartography and Geoinformatics, Faculty of Geography, 119991 Moscow, Russia
[h] University of Potsdam, Institute of Geosciences, 14476 Potsdam, Germany

ARTICLE INFO

Keywords:
Retrogressive thaw slump
Megaslump
Thermal denudation
Permafrost degradation
Batagay
Ground ice

ABSTRACT

Thaw slumps are clear indicators of rapid permafrost degradation. They form preferentially in near-surface ice-rich permafrost of northern high latitudes after initial thermal disturbance by the subsequent interplay of thermal (thawing of frozen deposits and melting of ice) and mechanical (slumping and erosion) processes. The largest known thaw slump on Earth – the Batagay megaslump – has been identified in sloping terrain on the Yana Upland in northern Yakutia. Its initiation began in the 1980s, with a current area of >0.8 km^2. It continues to grow and has headwall retreat rates of up to 15 m per year. While various satellite remote sensing studies of the Batagay thaw slump have been undertaken, on-site studies characterizing internal landforms, terrain changes, and geomorphic processes have not yet been conducted. To fill this knowledge gap and to enhance our understanding of the dynamics of very large thaw slumps, our study employs on-site observations and detailed permafrost sampling combined with unoccupied aerial vehicle data from 2019. The latter were used to generate an orthomosaic, a digital surface model, hypsometric slope profiles and a map of relief types in the thaw slump. Within the Batagay thaw slump, the dynamic relationship between headwall morphology and slump floor is largely determined by the cryolithological structure of the permafrost horizons exposed across the headwall rising up to 55 m above the slump floor. Factors include the thickness and overall high volumetric ground-ice content (up to 87 %) of the cryostratigraphic horizons. Furthermore, the diurnal and seasonal insolation exposure of the headwall perimeter superimposes both thermal denudation activity and meltwater transport of eroded material. Thus, recent degradation patterns are linked to permafrost properties. Therefore, the Batagay thaw slump is not only a window into Earth's past as it reveals ancient permafrost, but its modern dynamics highlight that ongoing rapid permafrost thaw under present Arctic warming is directly influenced by its Quaternary geological and permafrost history.

1. Introduction

The study of the permafrost state, the dynamics of cryogenic processes, and associated terrain changes is especially relevant in the context of modern climate change, which is largely amplified in the Arctic (Cohen et al., 2014; Barnes and Polvani, 2015; IPCC, 2021). Increasing summer air temperatures and seasonal thaw depths (Streletskiy et al., 2015; Romanovsky et al., 2017; Biskaborn et al., 2019; Vasiliev et al., 2020) in combination with a high ground-ice content activate a number of cryogenic processes inducing topographic changes,

* Corresponding author.
E-mail address: akizyakov@mail.ru (A.I. Kizyakov).
[1] Current address: Technische Universität Dresden, Institute of Geography, 01069 Dresden, Germany.

https://doi.org/10.1016/j.geomorph.2022.108501
Received 8 September 2022; Received in revised form 18 October 2022; Accepted 19 October 2022
Available online 22 October 2022

which potentially threaten surface stability and – if present – human infrastructure. Such cryogenic processes comprise thermal denudation, thermal erosion, thermal abrasion, and thermokarst (e.g. Grigorev et al., 2009; Günther et al., 2013; Costard et al., 2014; Kanevskiy et al., 2016; Nitze et al., 2020).

In areas with near-surface massive ground ice (tabular ground ice or large ice wedges) or other ice-rich permafrost, retrogressive thaw slumps (RTS; e.g., Burn and Lewkowicz, 1990), shortly named as thaw slumps, are formed. These large hollow-shaped degradation features are named as thermocirques (e.g. Voskresensky, 2001). Thermocirques, with a semicircular shape of the upper edge, form on slopes due to occasional surface disturbance or climate-induced deepening of the seasonally thawed (active) layer at sites with near-surface massive ground ice. In areas where ice-rich permafrost of late Pleistocene age – called the Yedoma Ice Complex – occurs, thermal terraces are one of the main landforms of thermal denudation at the shores of seas, rivers and lakes (Are, 1980, 2012). Unlike thermocirques, thermal terraces are formed due to the combined effects of coastal erosion and thermal denudation at coastal or shore bluffs (Leibman et al., 2008). For large thaw slump landforms, exceeding areas of 0.2 km^2, the term megaslump has been introduced by Lacelle et al. (2015). Given the existing terminological differences in the scientific literature, in the present study the term thaw slump is used.

Ice wedges form by the repetition of frost cracking of the frozen ground in winter and filling of the frost crack by spring snow melt which refreezes and forms vertical ice veins (Lachenbruch, 1962). By long-term annual repetition of cracking, filling and sub-surface freezing, and ongoing sedimentation, ice wedges grow (syngenetically) in both directions, vertically and horizontally. Ice-wedge growth further includes ice uplift due to temperature-related volume expansion of sediments forming the ridges of ice-wedge polygons (Konishchev and Maslov, 1969; Romanovsky, 1977). Ice Complex (Yedoma) deposits formed during tens of thousands of years in the late Pleistocene, contain large polygonal ice wedges up to 6–7 m wide and in places >40 m deep, and are widespread in Siberia and North America (e.g. Schirrmeister et al., 2013; Strauss et al., 2021). Yedoma Ice Complex permafrost is extremely ice-rich with high volumetric ice contents up to 80 % or more (Ulrich et al., 2014; Fuchs et al., 2020) comprising both intra-sedimental ice and wedge ice.

Thaw slumps are formed as a result of the combined effect of several cryogenic relief-forming processes on icy sediments. The interplay of thermal denudation, abrasion and erosion as well as thermokarst and slope processes fosters thaw-slump formation and dynamics at different stages of initiation, progression and stabilization (Are, 1980; Maksimov, 1984; Voskresensky, 2001; Leibman and Kizyakov, 2007).

If massive ground ice is exposed in thaw slump headwalls, thermal denudation includes the melting of the ice bodies and the thawing of enclosed frozen sediments, while combined gravitational and erosional processes promote mobilization of the thawed material in mudflows and landslides as well as by meltwater streams (Zhigarev, 1975; Are, 1980). If ground ice is temporarily buried by collapsing sediments or complete thawing of ice-rich sediments, the set of active relief-forming processes changes. This way, thaw slumps pass into the stage of landslide cirques, which are landforms with gentle slopes, significantly lower growth rates and smaller volumes of mobilized material (Leibman et al., 2014). At this stage, the change in the relief of these landforms occurs due to detachment slides of the active layer, solifluction and frost creep. A stabilization stage is reached when sediment accumulation (cover) exceeds the active layer depth and lasts until covered or exposed ground ice melts again. Large thaw slumps are polycyclic forms with alternating stages of active growth and temporary stabilization (Lantuit et al., 2012).

The resulting landforms of permafrost thaw are extremely dynamic. The lateral growth rates of thaw slumps reach up to a few tens of meters per year (Lantuit and Pollard, 2008; Kizyakov, 2005; Lantuit et al., 2012; Günther et al., 2013; Ward Jones et al., 2019; Leibman et al., 2021). Intensive permafrost degradation accompanied by the release of organic matter and greenhouse gases leads to changes in adjacent ecosystems (Lantuit and Pollard, 2005; Kokelj et al., 2009; Cassidy et al., 2017) and have a positive feedback on Arctic warming (e.g. Koven et al., 2011; Turetsky et al., 2020).

To map RTS distribution and explore their dynamics, on-site field data (Burn, 2000; Leibman and Kizyakov, 2007; Khomutov et al., 2017) and radar and optical remote sensing data (Lantuit and Pollard, 2005; Lantz and Kokelj, 2008; Kokelj et al., 2015; Séjourné et al., 2015; Nitze et al., 2018; Bernhard et al., 2022) have also been used in different regions. Airborne data from aerial vehicles, including unoccupied, were used to create detailed digital surface models (DSM) of RTS (Swanson and Nolan, 2018; Van der Sluijs et al., 2018). Algorithms for automated search and identification of surface disturbances associated with cryogenic landslides and thaw slump formation are currently being developed based on the analysis of remote-sensing data with machine learning methods (Brooker et al., 2014; Nitze et al., 2021; Runge et al., 2022).

A significant amount of data on the structure, conditions of occurrence, and dynamics of thermal denudation and growth of thaw slumps has been obtained on Herschel Island at the Yukon coast (Lantuit and Pollard, 2005, 2008), in northern continental Alaska and Canada (Lantz and Kokelj, 2008; Lacelle et al., 2015), in the Canadian Arctic Archipelago (Ward Jones et al., 2019), in the European North of Russia (Kizyakov et al., 2013), the North of West Siberia (Kizyakov, 2005; Khomutov et al., 2017; Leibman et al., 2021), on the Arctic coastal plains and in the central parts of Yakutia (Grigoriev, 2008, 2019; Pizhankova and Dobrynina, 2010; Pizhankova, 2011; Günther et al., 2013, 2015a, 2015b; Shepelev et al., 2020; Tumskoy et al., 2021).

The present study analyzes the morphology of the terrain within the large Batagay thaw slump, located in the northern part of Yakutia, north-eastern Siberia. The history of the origin and development of this feature based on a series of satellite images is considered in Kunitsky et al. (2013), Günther et al. (2015b), Savvinov et al. (2018), and Vadakkedath et al. (2020).

We employ airborne data combined with on-site observations and sampling of the vertical headwall of the Batagay thaw slump to (1) determine the morphology and dimensions of the largest recent permafrost thaw feature on Earth by using UAV data; to (2) characterize degradation pattern within the thaw slump depending on cryostratigraphy, ice content and exposition of the headwall; and to (3) discuss past, current and future dynamics of Batagay permafrost degradation and potential impacts of accelerating thaw-related terrain changes in the area.

2. Study area

The Batagay thaw slump (67.58°N, 134.77°E) also known as the Batagaika megaslump or as Batagaika crater, is located in the Yana Uplands, which belong to the Yana-Oymyakon mountain region of interior Yakutia (Fig. 1). Here, strongly continental climatic conditions are reflected in low precipitation (mean annual precipitation (MAP) of 203 mm, 1988–2017) and high annual air temperature amplitudes between −40 °C in winter (mean Dec–Feb) and 13.7 °C in summer (Jun–Aug) at a mean annual air temperature (MAAT) of −12.4 °C (period 1988–2017; Murton et al., 2022). Since 1950, the MAAT has increased by >2 °C and the MAP by >50 mm (Savvinov et al., 2018).

The permafrost occurs in continuous distribution, reaches ~300 to 500 m thickness and the mean annual ground temperature varies from −9 to −7 °C at the depth of zero annual amplitude (Geocryological Map of the USSR, 1996). The thickness of the active layer ranges from 0.8 to 1.4 m, depending on vegetation type (Shestakova et al., 2021). The modern taiga vegetation is dominated by *Larix gmelinii* (larch) and *Pinus pumila* (dwarf pine) in higher reaches of the mountains, and includes *Betula exilis*, *B. divaricata* and sparse *B. pendula* (birches). Lichen and moss cover is common, while mountain grasses and herbs are sparse (Ashastina et al., 2018; Savvinov et al., 2018).

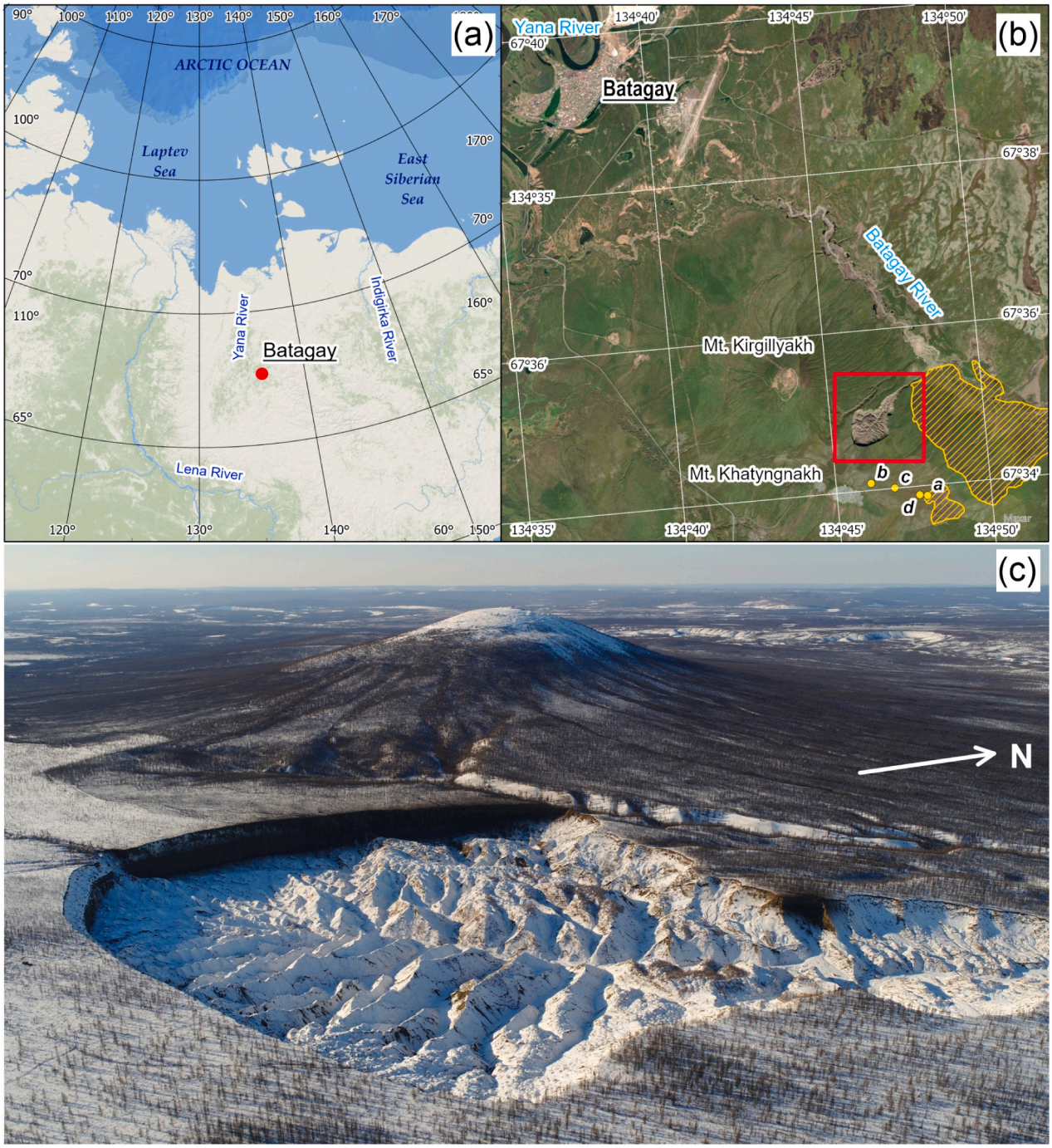

Fig. 1. Location of the Batagay thaw slump (a) on the Yana Upland in North-eastern Siberia, (b) in the vicinity of Batagay settlement and (c) shown as aerial view in spring 2019, note Mount Kirgillyakh in the background. In (b) the locations of the field photo points presented in Fig.12 are shown and areas of wildfires 2018–2019 are indicated with hatched yellow fill.

In 2019, the Batagay thaw slump was about 1800 m long and 890 m wide and has been growing since then. It is located on the east-facing hillslope of the saddle between Mount Kirgillyakh (590 m above sea level; a.s.l.) and Mount Khatyngnakh (380 m a.s.l.); about 10 km south of the village of Batagay (Fig. 1b). The widening of a pre-existing gully (thermal erosion ravine) into a distinct slump form was firstly recognized on satellite imagery of 1991 (Kunitsky et al., 2013). The average growth rates at different sites of the feature reached 7–15 m per year in 2004–2010 (Kunitsky et al., 2013). The recalculation of area loss data given by Vadakkedath et al. (2020) revealed annual growth rates of 11.3 to 14.9 m per year in 1991–2018.

The headwall between the slump floor and the surface in its western part reaches up to about 55 m height and exposes a series of ancient permafrost deposits. The lowermost horizon of mid-Pleistocene age is regarded as the second oldest directly dated permafrost in the Northern Hemisphere (Murton et al., 2022). Following Murton et al. (2022), the headwall exposes six cryostratigraphic units – from the floor to the top – named as the Lower Ice Complex (Marine Isotope Stage (MIS) 16 or earlier), the Lower Sand Unit (some time between MIS 16 and 6), the Woody Layer (MIS 5; in places present as up to 3 m thick lenses), the Upper Ice Complex (MIS 4–2), the Upper Sand Unit (MIS 3–2) and the Holocene Cover on top (MIS 1). The ancient permafrost exposed in the

Batagay thaw slump has already been the subject of several paleo-environmental studies (e.g. Ashastina et al., 2017, 2018; Murton et al., 2017; Opel et al., 2019; Vasil'chuk et al., 2019, 2020; Courtin et al., 2022; Jongejans et al., 2022).

3. Materials and methods

3.1. Fieldwork

Data and samples were acquired during joint Russian-German fieldwork at the Batagay thaw slump from 18 March to 4 April 2019 (Jongejans et al., 2021). Continuous sampling of frozen sediments and ground ice along the ~55 m deep western headwall was conducted on climbing rope and complemented by selected sampling sites on the slump floor and slopes which allowed for capturing the entire exposed permafrost inventory and for obtaining representative sample material from all exposed cryostratigraphic units for sedimentological, biogeochemical, isotopic and dating approaches. Sampling profiles were conducted at the snow-free western part of the headwall in sections I and II (Fig. 2). The sampling profiles were sketched and photographed and the

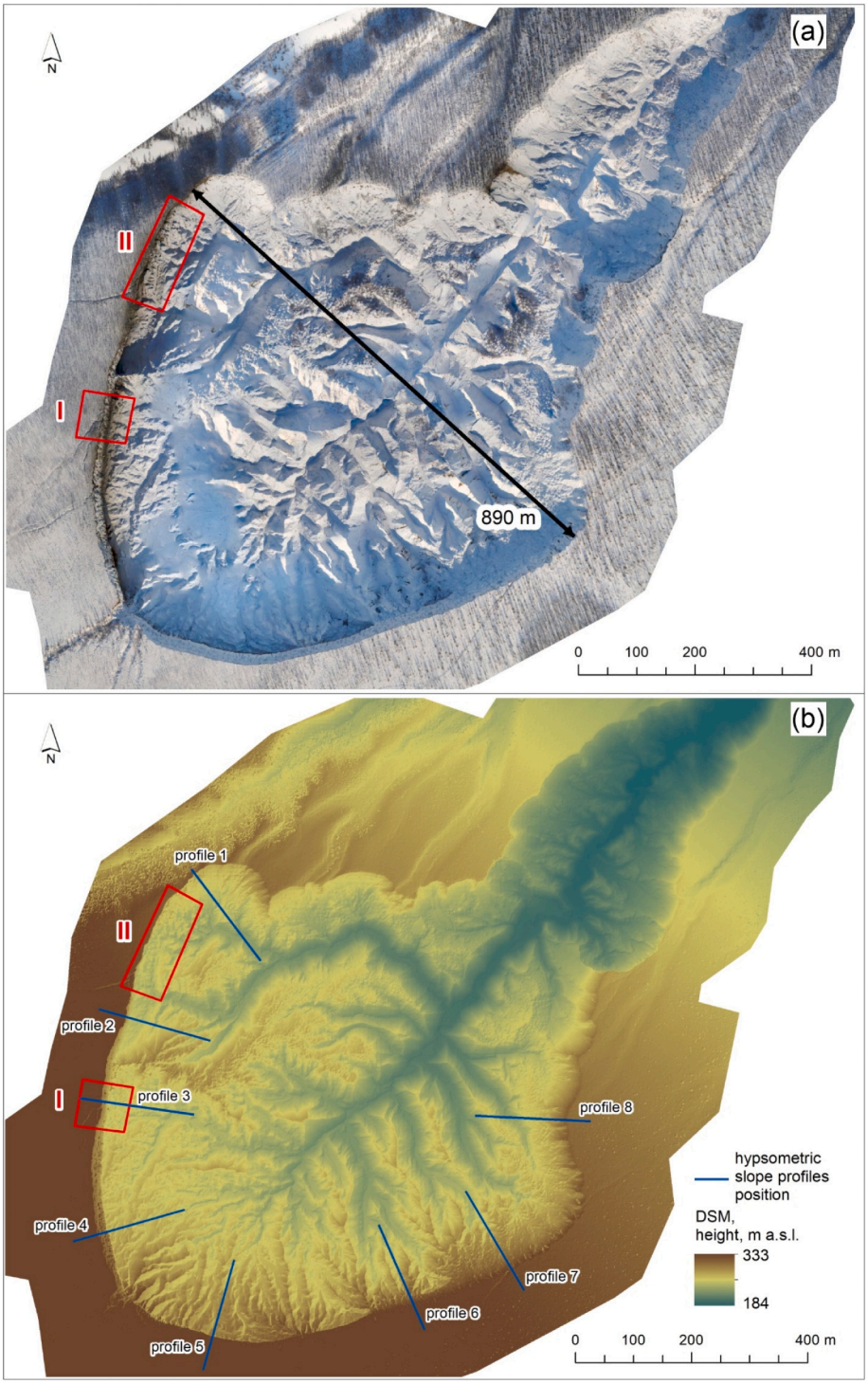

Fig. 2. The Batagay thaw slump shown (a) as orthomosaic and (b) as digital surface model based on 2019 data. The red rectangles mark the position of the sections I and II for which the calculation of ice content was performed.

material was cryolithologically described (Jongejans et al., 2021) following the terminology by Kudryavtsev et al. (1979), partly presented in French and Shur (2010). All samples were kept frozen upon return to the laboratories at the Melnikov Permafrost Institute SB RAS Yakutsk (Russia) and the Alfred Wegener Institute Potsdam (Germany).

3.2. UAV survey and processing

The UAV surveys during the field campaign resulted in airborne imagery of the entire slump including the headwall and the floor. We used a DJI Phantom 4 Advanced drone to take high-resolution imagery of the thaw slump. The camera onboard the UAV was equipped with a 1-in. 20-megapixel CMOS sensor and the camera had an f/2.8 wide-angle lens with a 24 mm-equivalent focal length. Various camera orientations were used, including vertically downwards to capture the topography of the thaw slump as well as perspective or oblique photos and horizontal (perpendicular to its vertical extent) photos of the headwall to identify features of the exposed cryolithological horizons. Imagery post-processing was undertaken using the Agisoft Photoscan software and following this, an orthomosaic (Fig. 2a) and a digital surface model (DSM) with spatial resolution of 0.12 m (Fig. 2b) were created.

3.3. Ground ice volume

A thorough cryolithological description and sampling of frozen sediments and ground ice exposed in the headwall of the thaw slump was performed in its western part (Fig. 2a, sections I and II). In this part of the headwall, horizons of the cover deposits, the Upper Ice Complex (IC), the Upper Sand, the Lower Sand and the Lower IC are present. These cryostratigraphic horizons were distinguished in previous studies (Murton et al., 2017, 2022).

The assessment of the total ice content in sections I and II is based on the analysis of photographs from the UAV for wedge-ice abundance and the results of laboratory determination of the gravimetric ice content of the sediment samples totaling 77 determinations (Table 1) for intra-sedimental ice. The total volumetric ground ice content (TVIC) of the cryostratigraphic horizons exposed in the Batagay megaslump was estimated by eq. (1) after Grechishchev and Shur (1990):

$$\mathrm{TVIC} = \mathrm{WIV} + \mathrm{VICS} \times (1 - \mathrm{WIV}), \quad (1)$$

where WIV–wedge-ice volume, unit fraction; VICS – volumetric ice content of sediments between ice wedges, unit fraction.

To calculate the visible proportion of wedge-ice in the walls of the outcrop, we used a series of UAV imagery taken perpendicular to the wall from the middle of its height. We took the calculated area ratio between ice wedges and the entire section as the wedge-ice volume (WIV), following Kanevskiy et al. (2016) who could verify this simple approach by repeated analysis of the same study site over several years. We take into account that due to the cutting plane of the outcrop, fixed on our image snapshots, there can be both slightly overestimated and underestimated values of WIV, depending on how the ice wedges are exposed by the retreating headwall. Due to the considerable analyzed area of the outcrop in the headwall (section I: ca. 55 m × 84 m (Fig. 3); section II: ca. 55 m × 194 m), we here assume that we obtained average values that characterize the WIV of the cryolithological horizons well.

To calculate the volumetric ice content of sediments between ice wedges (VICS) based on the results of laboratory data on gravimetric ice content of the sediment samples, we used the Eq. (2) after Tsytovich (1973) and Grechishchev and Shur (1990):

$$VICS = \frac{\rho \times (W_{tot} - W_w)}{\rho_i \times (1 + W_{tot})}, \quad (2)$$

where ρ – density of frozen sediments; ρ_i – density of ice; W_{tot} – total water content of frozen sediments (relative to dry sediments); W_w – unfrozen water content.

Permafrost sampling was undertaken within section I in two vertical profiles at the headwall and at selected sampling sites on the slump floor and slopes. The results of the laboratory ice content determination were extrapolated to the same cryolithological horizons within section II. All sampled sediments are either fine sand or coarse silt. The density of frozen sediments (ρ) of such deposits equals 1500 kg/m^3 on average (Tsytovich, 1973). The density of ice (ρ_i) equals 917 kg/m^3 (e.g., Harvey, 2014). The total moisture content of frozen sediments (W_{tot}) was determined as the gravimetric ice content of the sediment samples by measuring the difference in weight percentage (wt%) between wet (frozen) and dry weights after freeze-drying (Subliminator 3–4–5, Zirbus Germany). Averaged values for each of the cryolithological horizons were used (Table 1). Taking into account the textural composition of sediments and the low ground temperature, which determine the extremely small possible amounts of unfrozen water, we estimated the moisture content due to unfrozen water (W_w) as 0.01.

Further in this paper, when separating and naming horizons in the outcrop, we use cryolithological boundaries based on presence and volume of ice wedges. These cryolithological boundaries do not necessarily correspond to (cryo-)stratigraphic boundaries and hence, our cryolithological horizons used in this paper may slightly differ from the cryostratigraphic units as defined by Murton et al. (2022).

Table 1
Ice content values of cryolithological horizons exposed in sections I and II at the western headwall are given as wedge-ice volume (WIV), volumetric ice content of sediments between ice wedges (VICS; mean ± standard deviation) and the total volumetric ice content (TVIC). Number of samples VICS calculation (N) are given in brackets.

	VICS [%]	Section I		Section II	
		WIV [%]	TVIC [%]	WIV [%]	TVIC [%]
Upper Ice Complex	56.4 ± 11 ($N = 46$)	70.2	87	62.9	83.8
Upper Sand	50.8 ± 10 ($N = 6$)	Not exposed		7.6	54.6
Lower Sand	46.9 ± 7 ($N = 20$)	5.7	50	13	53.8
Lower Ice Complex	53.2 ± 8 ($N = 5$)	55.5	79.2	Not exposed	

3.4. Thaw slump morphology

To analyze the topography of the thaw slump's floor and slopes, the UAV-derived DSM and field photos were used. A classification of the surface steepness and the dissection of the relief (i.e. the range of changes in surface height in the DSM within a moving window of 10 × 10 m) was done in QGIS and ESRI ArcGIS. Using ArcGIS 3D Analyst tools, hypsometric profiles were derived from the DSM. Using ArcGIS 3D Analyst tools, hypsometric profiles were derived from the DSM. In order to assess incoming solar radiation (insolation) and its relative distribution within the thaw slump, insolation patterns were analyzed using the DSM and Spatial Analyst tools in ArcGIS for a selected representative day during the spring season (1 April as a day within our fieldwork) and cumulative insolation for a whole year with the standard setting of 0.3 overcast conditions. As a result, these insolation estimations provide an insight into spatial patterns of areas with low and high amounts of incoming solar radiation.

4. Results

4.1. Characteristics of the cryolithological horizons described from top to bottom

*The **cover layer*** reaches a thickness of 1–3 m and covers the

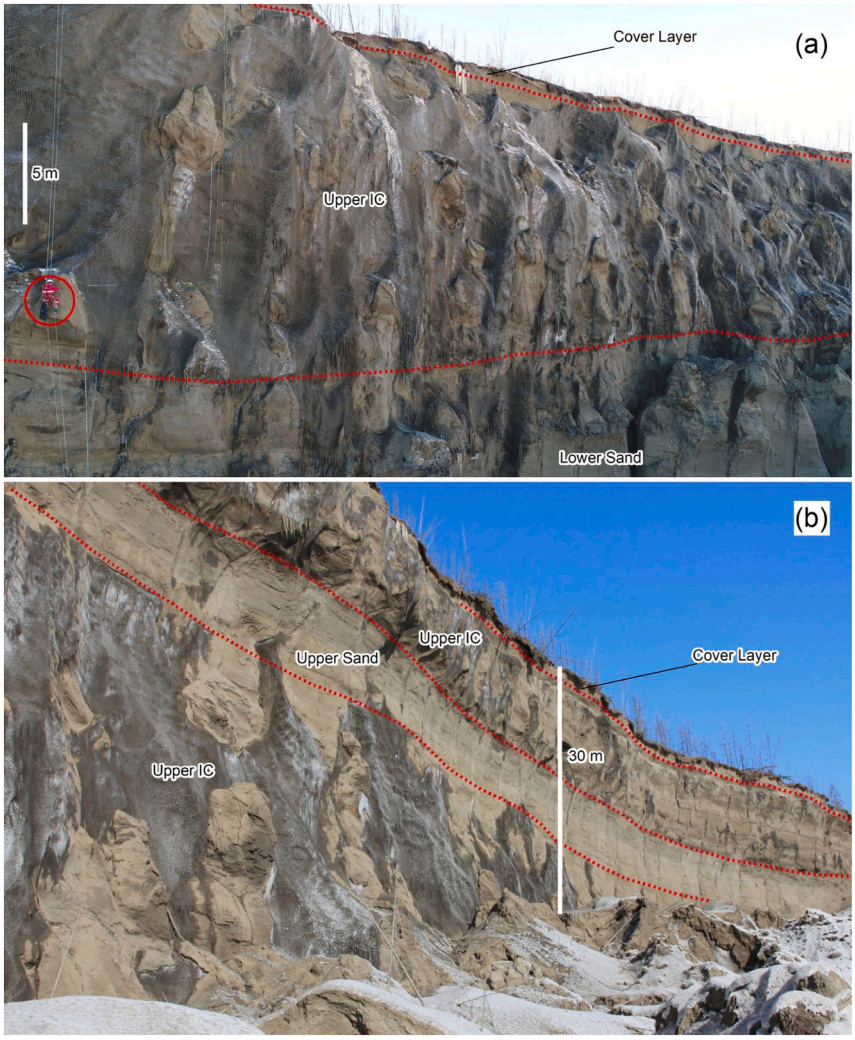

Fig. 3. Outcrop of the Upper IC in section I (a) and the Upper Sand in section II (b). Cryolithological boundaries are marked as dotted red lines. A person on climbing ropes is circled in red for scale in (a).

surrounding surface, including the slope into which the thaw slump is cutting (section I, Fig. 3). The thickness of this cover layer above the Upper Ice Complex varies along the section with local depressions of the base. No ice wedges have been observed in the cover layer. The cover layer includes the active layer and an underlying transient layer that alternates in status between seasonally frozen ground and permafrost over sub-decadal to centennial time scales (Shur et al., 2005). It is composed of yellowish-gray very fine sand with predominantly massive (not visible) cryostructures. The sediments are characterized by well-defined layers with individual dark brown lenses, enriched in organic matter that shows cryostructures with multiple isolated ice aggregations. A ferruginous horizon with a thickness of 15–20 mm is present. In the transient layer, interbedding of sandy horizons with massive cryostructures and sandy loam with lenticular and layeredcryostructures is found. The active layer contains a large number of tree and shrub roots. The entire cover layer is distinguished from sediments of the underlying Upper IC by a brighter coloration and the presence of bright red ferruginous lenses.

The ***Upper Ice Complex*** (***IC***) is exposed at the headwall at a varying depth range. The upper boundary of the Upper IC was found at 1–3 below the surface (b.s.) and the lower boundary at 27–29 m b.s. This horizon is characterized by very large ice wedges penetrating its entire thickness (section I, Fig. 3; see also Fig. 4a and b). Upper IC deposits are exposed almost along the entire perimeter of the headwall with distinct changes in the north-western part of the headwall, where the Upper Sand with thin composite sand-ice wedges is wedged into the Upper IC, which in this part increases its vertical dimension due to its dipping base (section II, Fig. 4c). The Upper IC ice wedges are classic polygonal features composed of vertically stratified ice veins with inclusions of mineral and organic particles. Between the ice wedges, former polygon centers of frozen very fine sand of light-brown and brown color are present.

The upper part of Upper IC is a complex layered sandy loamy stratum with ice schlieren (thin lenticular layers of segregated ice of various orientations in frozen ground). The inclined and horizontal layered ice schlieren are 1.5–70 mm thick and lenticular and massive cryostructures occur between the schlieren. Below, occurs predominantly fine sand with massive or thin-layered cryostructures (thin ice lenses 0.1–0.5 mm thick and the same sandy loam interlayers) interbedded with horizons with reticulate and lens-like braided cryostructures.

The ***Upper Sand*** is exposed to a limited extent at the northern end of the western headwall (section II, Fig. 4c) and at the southeastern wall (Opel et al., 2019), which was covered by snow in spring 2019. At section II, the Upper Sand is embedded in the Upper IC. The maximum thickness of the Upper Sand layer is 7–8 m. It is overlain by the Upper IC and the cover layer, which sum up to a total thickness of 9–11 m. The Upper Sand layer is penetrated by narrow composite sand-ice wedges, visually <30 cm wide. Partly, these composite wedges appear to grow in

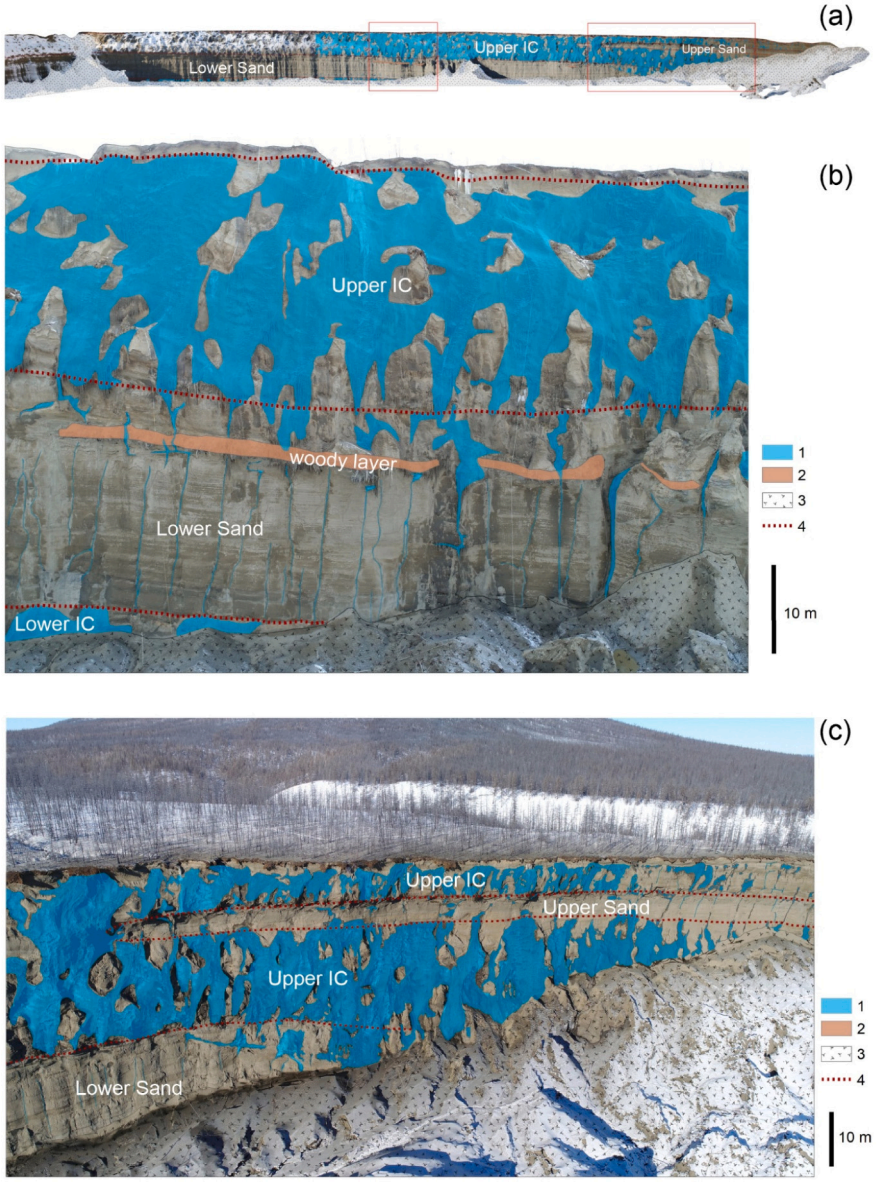

Fig. 4. Visible ice wedges in the western headwall (a) and detailed in section I (b) and section II (c): (1) ice wedges (shaded in blue), (2) woody layer, (3) slump floor, debris cones, (4) cryolithological boundaries.

the same cracking positions as the ice wedges of the Upper IC below and above and are connected to those now. During field work, the Upper Sand deposits in the headwall outcrop were not described and sampled. The respective samples were taken from a baydzherakh (thermokarst mound) located at the foot of the headwall built of Upper Sand deposits. The Upper Sand is light-brown fine sand including sparse gravel (up to 0.5 cm in diameter). The cryostructure is lenticular with 0.5 mm thick and 10–50 mm long ice lenses.

Substantial parts of the western headwall are composed of the ***Lower Sand***, vertically exposed with a thickness of about 20 m (Fig. 5). In its uppermost part, the Lower Sand exhibits a distinct feature: a clearly gravelly orange layer seen along the entire thaw slump along the open walls of the Lower Sand and discontinuous pockets or lenses of woody debris marking the position of the ***Woody Layer***. The deposits of the Woody Layer are gray and light-brown silty sands with reddish ferruginous spots and include numerous organic remains, peaty lenses, in-situ rootlets and wood (0.5–10 cm in diameter). The cryostructures are lenticular (ice lenses 0.5–2 mm thick and 5–10 cm long) or layered (single ice layers 1 mm thick and 10 mm apart). Around peat lenses, the cryostructures form larger ice lenses (2–20 mm thick, up to 1 cm long and 20–50 mm apart) with lenticular cryostructures (ice lenses 0.5 mm thick and 1–2 mm long) between the ice layers. The Woody Layer marks an erosional surface and paleo surface (Murton et al., 2017) and does not contain any ice wedges. The underlying Lower Sand is composed of partly layered light-gray and light-brown fine sand with rare gravel inclusions (2–5 mm in diameter). Numerous in-situ rootlets and rare wood remains (up to 5 cm long and 1 cm in diameter) are present. The cryostructure is either massive or lenticular (0.5 to 1 mm thick and 5 to 10 cm long ice lenses). Narrow composite wedges (10 to 20 cm wide) across this entire horizon contain alternating ice and sediment veins (up to 2 mm wide).

The lowermost exposed stratigraphic horizon is the ***Lower Ice Complex***. It is only exposed in ection I right above the slump floor and reaches up to 1.5 m thickness here. It is composed of fine light-gray and brown sandy silt with small shale fragments originating from the underlying diamicton (Murton et al., 2017) as well as in-situ rootlets and organic black spots (in the lower part). Cryostructures are microlenticular or massive resulting in a low intra-sedimental ice content.

Fig. 5. Lower part of the western headwall, mainly built of Lower Sand underlain by the lower IC and topped by the Woody Layer. Cryolithological boundaries are marked as dotted red lines. A person on climbing ropes is circled in red for scale.

Truncated ice wedges of the Lower IC reach visible thicknesses of 1.2 m up to 3.5 m and widths of 0.6 m up to about 1 m. In places, significant amounts of wood, buried pool ice, vertical ice veins and small composite wedges can be found in the ice-rich sediments, likely attributed to erosional structures within the Lower IC. A reddish ferruginous erosional gravel layer tops the Lower IC.

4.2. Ground-ice content throughout the sections

During the survey period in March–April 2019, the contours of ice wedges and enclosing sediments of the Upper IC were confidently distinguished only on the western part of headwall (east-facing) due to its insolation and the early snowmelt. The walls of the northern and western exposures were still partially covered with snow (Fig. 4a), which made it difficult to determine the exact percentage of ice content. However, as the same cryolithological horizons are distinguished across the entire headwall of the thaw slump, we assume the ice content values from the studied sections are characteristic for the respective stratigraphic units. At the same time, we note that toward the northern end of the western wall, where the Upper Sand appears, the general structure of the wall section and its ice content change. Toward the northern extremity of the wall, Upper IC ice wedges practically disappear (Fig. 4c). This is the only significant change in ice content recorded along the exposed headwalls.

The TVIC was calculated for two sections of the western wall (Figs. 2c, 4a). Within section I (Fig. 4b), in the field we made a thorough vertical sampling profile of the wall covering the Upper IC, Lower Sand (including the Woody Layer), and the Lower IC. In section II (Fig. 4c), the TVIC was calculated for deposits of the Upper IC, Upper Sand, and Lower Sand.

The VICS is higher for the Ice Complex units (Upper IC: ca. 56 %; Lower IC: ca. 53 %) compared to the sand units (Upper Sand: ca. 51 %; Lower Sand: ca. 47 %). More differentiation is seen in the wedge-ice volume (WIV) of the respective cryolithological horizons, where the largest shares of wedge ice were observed in the Upper IC (ca. 63–70 %) and the Lower IC (ca. 56 %), while the sand units contain up to ten-fold lower WIV in the Lower Sand (ca. 6–13 %) and the Upper Sand (ca. 8 %) (Table 1). Consequently, the resulting TVIC is highest for the Upper IC (ca. 84–87 %) and the Lower IC (ca. 79 %), while for the sand units it varies only between about 50 and 55 % (Table 1).

4.3. Thaw slump main dimensions

The orthomosaic and the DSM of the Batagay thaw slump (Fig. 2a and b) allowed the morphometric characteristics of the thaw slump – as surveyed in spring 2019 – to be established. The maximum width of the thaw slump in its upper bowl-shaped part was 890 m. The maximum height of the headwalls from the edge to the slump floor underneath was 55 m in the western part of the thaw slump. As the thaw slump cuts into the gentle east-facing slope of the saddle between Mount Kirgillyakh and Mount Khatyngnakh, the heights along the headwall edge of the bowl-shaped main part of the slump span from 275 to 319 m a.s.l. The minimum heights within the slump floor are localized in the valley of the main erosion cut. In the central bowl-shaped part, the minimum height is 207 m a.s.l.

4.4. Slope profiles

The transverse slope profiles (Fig. 2b) along the western wall (profiles 1–3 in Fig. 6a–c) represent almost sheer vertical walls, in places even exhibiting overhangs, where the lower part of the vertical wall, composed of the Lower Sand, is below the “cornice” of the overhanging Upper IC deposits. The Lower Sand forms straight walls, practically without deviations from the vertical. On the western wall in the area covered by profiles 2 and 3, the maximum height difference between the upper wall edge and its foot reaches 50–52 m.

The northernmost profile (profile 1; Fig. 6a) crosses the headwall where only composite wedges of the Upper Sand are present. Nevertheless, a fragment of the vertical wall remains, at the foot of which debris accumulated. As the ice-poor deposits of the Upper Sand predominantly exposed here produce only little meltwater amounts upon thaw, the thawed material cannot be transported away from the foot of the wall, and the height of the outcrop gradually decreases over time.

Moving toward the southwestern part of the thaw slump (profiles 4 and 5; Fig. 6d–e), a concave upper part is noted in the transverse profile of the walls within the outcrop of the Upper IC. A possible explanation

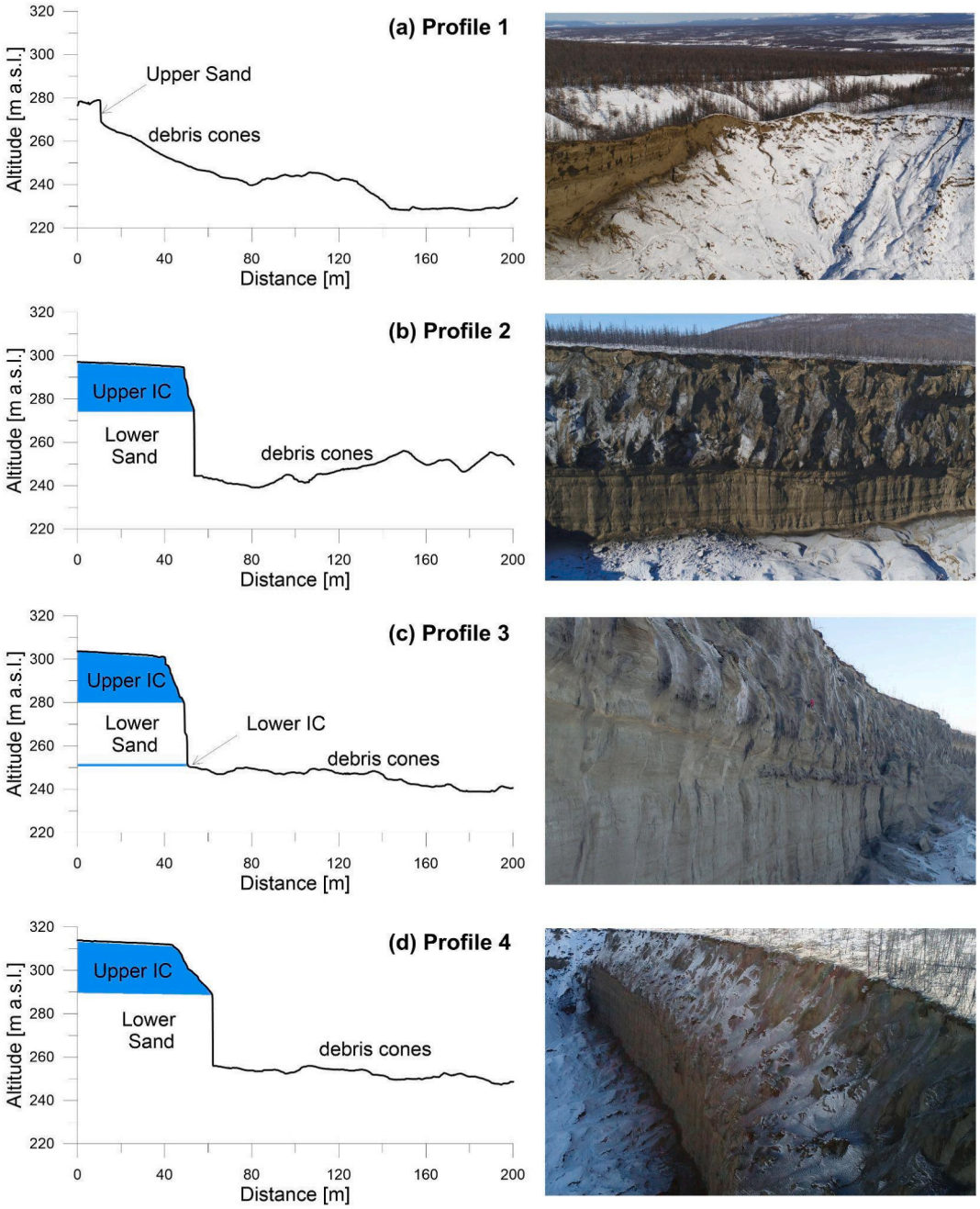

Fig. 6. Hypsometric slope profiles (profiles 1 to 8; left) and corresponding aerial views from different parts of the Batagay thaw slump (a to h; right). Profile positions are given in Fig. 2b.

for this is a change in insolation exposure of the wall in the southwestern part due to the bowl-like shape of the thaw slump (Fig. 7). The upper part of the outcrop continues to be exposed to the sunlight and retreats more intensively, while the lower part is in the shade and the rate of thermal denudation decreases.

Within the southern and eastern walls of the thaw slump, we observe a gradual decrease in the exposed headwall height, as the lower parts are increasingly covered by debris cones. At the southern part, the debris forms cones directly below the base of the ice-rich sediments of the Upper IC (profile 6; Fig. 6f). Further to the east (profile 7; Fig. 6g) where the Upper Sand overlies the Upper IC (Opel et al., 2019), the slumped material partially covers the outcrop as well as the slopes around profile 8 (Fig. 6h), which is almost completely covered by slumped material. At the same time, flattening of the slopes is observed, but the surface is structured by baydzherakhs (thermokarst mounds) and sediment blocks that slumped or collapsed from the upper edge. The low height position of the baydzherakhs in profile 8 (20–25 m below the thaw slump upper edge) may indicate the base of Upper Sand and thawed upper part of the Upper IC. If deposits of the Upper IC are present here in the thaw slump wall, they are covered by debris exceeding the active layer thickness.

4.5. *Thaw slump morphology*

The DSM, the derived information on slope inclination, and the vertical dissection of the terrain (Fig. 8a and b) made it possible to identify several distinct areas within the slump floor, differing in the

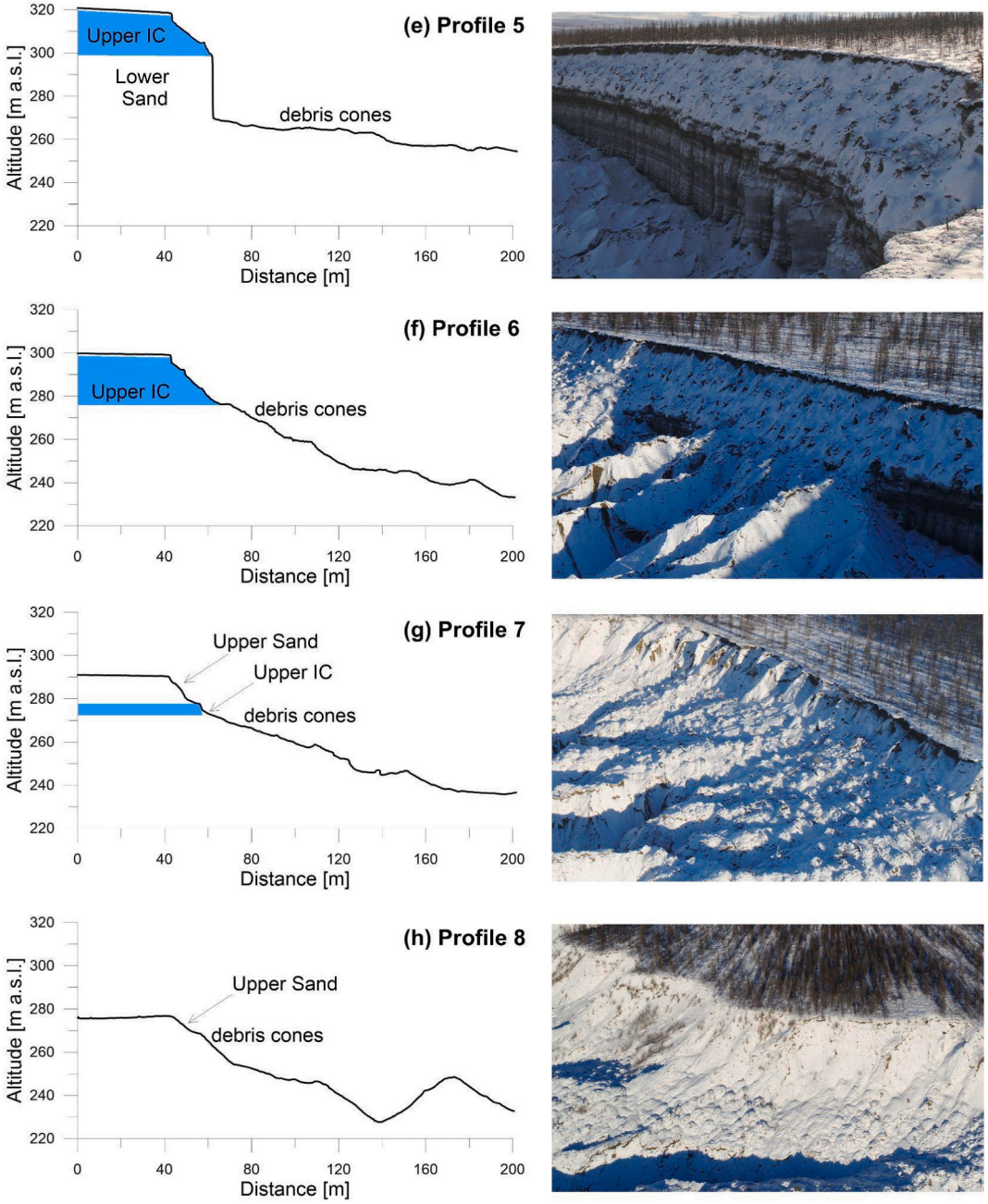

Fig. 6. (*continued*).

magnitude of the terrain vertical dissection and the morphology of landforms. The following three main relief areas (A–C) with in total five subtypes are identified on the slump floor (Fig. 8c). Further, main relief types of the thaw slump headwall (D–F) as well as the thalwegs of thermal erosion ravines (G) are distinguished (Fig. 8c):

(A) Terrain with strong surface dissection: Mainly ridges and incised valleys;
(B) Terrain with moderate surface dissection: Flattening, slightly dissected by erosion, the surfaces of the slopes descending from the edges of the thaw slump;
(C) Terrain with low surface dissection: Relatively leveled terrain in the floor of the thaw slump with residual hills, slightly modified by erosion (C-1); Elevated remnants in the floor of the thaw slump with a slight difference in terrain heights (C-2); Flattened areas directly adjacent to the western wall (C-3).

Based on field observations and DSM interpretation, we segmented the thaw slump edge and identified three types of headwall (Fig. 8c):

(D) Vertical walls with only a slight inclination in the upper part;
(E) Two-part profiles with an inclined upper part and a steep lower part;
(F) Concave steep slopes (without a vertical wall) in the upper part and flattening in the lower part.

Statistical data on the morphometric characteristics of the selected relief areas of the slump floor (A–C) are given in Table 2. We calculated the distribution of heights and the slope inclinations within the thaw slump floor at the foot of the headwalls. For a statistical assessment of the distribution of the terrain vertical dissection within the slump floor, a strip of variable width (30–40 m, according to the orientation of the pixel structure of the surface dissection scheme) along the vertical walls

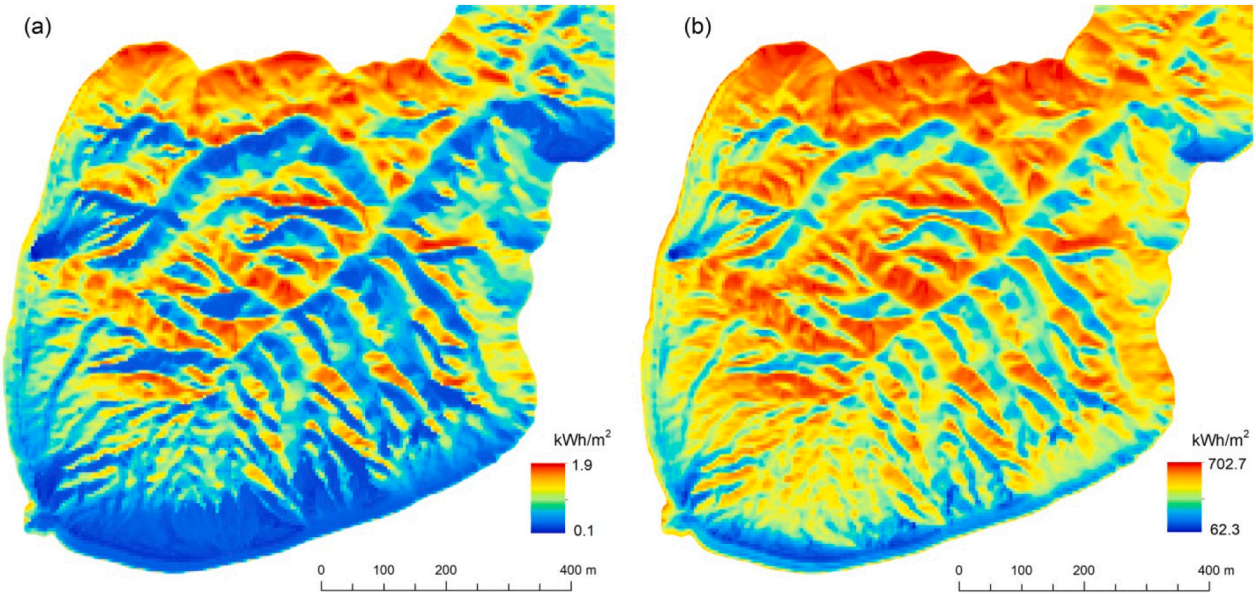

Fig. 7. Modeled solar insolation distribution within the thaw slump terrain. The scale bar characterizes amounts of incoming solar radiation due to the terrain's exposition and inclination (a) on April 01 and (b) for a whole year.

was cut out to eliminate the edge effect of the wall's influence on the statistics of dissection within the floor.

The highest values of vertical dissection are concentrated along the edge of the thaw slump. Along the western vertical wall, the height difference from the edge to the foot reaches 50–55 m. Two more sections of the thaw slump edge with vertical walls, but of much lower height (15–20 m), are located in its northeastern part, where the bowl-shaped part transitions into an extended erosional valley.

In the western part of the thaw slump floor, areas of average dissection of the terrain, relatively leveled terrain with residual hills, slightly modified by erosion (relief area C-1) are present. Within this area, the mean dissection of the relief amounts to 4.9 m, ranging from 2.3 to 9.8 m. The highest values are associated with a few ridges and erosion cuts.

Flattened areas (relief area C-3) adjoin directly to the western wall (Fig. 9). A ridge adjacent to the wall divides them in two parts. The mean of the vertical dissection here is 3.5 m, and the range of the value scatter is the lowest of all identified relief types due to the lowest maximum value of 7.3 m. The minimum heights within flattened areas are 235–240 m a.s.l., which is about 15–20 m lower than the surfaces of the remnants (relief area C-2) and 30–45 m below the tops of the ridges in relief area A.

The central part of the thaw slump is the oldest and most strongly dissected by erosion processes (relief area A). In this part of the slump floor, the average value of terrain dissection is 8.3 m with a range from 1.4 to 16 m. Linear anomalies with small values of terrain dissection are confined to the floors of large erosional valleys, sharply increasing on the sides. In relief area A, the highest values of the mean slope inclination reach 36°.

In the northwestern part of the floor is a fragment of elevated remnants with a small difference in surface heights (relief area C-2). According to the characteristics of the vertical dissection, with a mean value of 4.9 m as well as the height characteristics and the slope inclinations, this relief area corresponds to relief area C-1. However, C-2 differs from C-1 by the absence of linearly oriented erosion valleys and the spatial distribution of the variability of the slope inclinations (Fig. 8a), and seems to be closer to relief area B. Therefore, and because the C-2 area is distinguished from relief areas C-1 and B by clearly developed erosion valleys, we define it as a separate type of relief. The surface of the C-2 relief area is further structured by baydzherakhs of 4 to 8 m in diameter and 1–2 m high.

Along the periphery of the floor in the northern and eastern parts of the thaw slump stretches relief area B that also has a low average relief dissection of 5.9 m. However, unlike relief areas A, C-1 and C-2, there is no clear predominance of erosional dissection with the formation of pronounced ravines and ridges separating them. The mean slope inclination of 28° is also in the range of the A, C-1 and C-2 relief areas, but the relief area B exhibits concave slope surfaces, flattening down from the edge of the thaw slump.

4.6. Geomorphological analysis

The main process that determines ongoing headwall retreat and expansion of the Batagay thaw slump is thermal denudation – the thawing of permafrost, including ground-ice melt, and the collapse of the thawed material downslope. This so-called lateral denudation describes the permafrost degradation and slope retreat in a horizontal direction due to combined permafrost thaw and slope processes (Konishchev, 2009). Annually, the ice locally starts melting due to strong solar radiation directly affecting exposed ground ice in the walls in early spring (March–April) even at air temperatures far below 0 °C as noted during fieldwork in 2019 (Fig.7a).

We have further noted traces of block collapse of the Upper IC sediments (Fig. 9). Such failure of high and steep permafrost walls – in particular on coastal sea cliffs, but also in inland locations such as Batagay – occurs in areas where polygonal ice-wedges are widespread (e.g., Overduin et al., 2014; Günther et al., 2015a). The size of the collapsing blocks corresponds to the dimensions of the polygonal patterns delineated by the ice wedges. Gravity collapse occurs when the sedimentary polygon centers form an overhanging and protruding pinnacle around which the wedge ice has melted much deeper into the headwall surface. The shear resistance of sandy and silty frozen sediments is much higher than that of ice wedges. Therefore, the formation of cracks and the breaking-off of sedimentary blocks occur within the ice part.

In the warm continental summer season with air temperatures sometimes exceeding 30 °C, mudflows form at the foot of the thawing headwalls. Partially thawed and collapsed material accumulates near the slope, forming cones and ridges adjacent to the retreating wall. With a sufficient amount of water, this material is washed away, an erosional

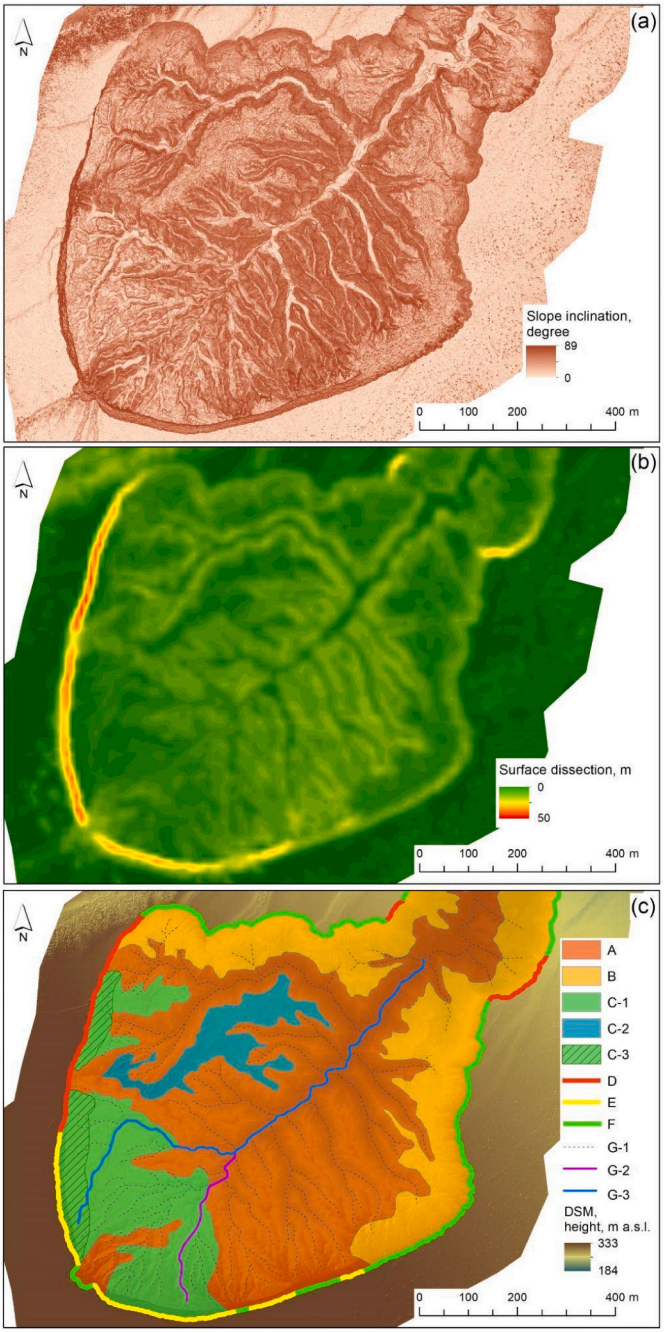

Fig. 8. Morphometric schemes of the thaw slump showing (a) slope inclination, (b) surface dissection and (c) relief types of the thaw slump floor and the walls. The relief types are distinguished as (A) terrain with a strong dissection; (B) terrain with medium dissection; (C-1) terrain with low dissection: floor of the thaw slump with residual hills; (C-2) terrain with low dissection: elevated remnants in the floor of the thaw slump; (C-3) terrain with low dissection: flattened areas directly adjacent to the western wall; (D) vertical walls with slight inclinations; (E) Two-part profiles with an inclined upper part and a steep lower part; (F) concave steep slopes; (G-1) thalwegs of erosion ravines, G-2 and G-3 thalweg lines for hypsometry profile on Fig. 11.

gully is formed, and then a ravine, through which the material is carried beyond the thaw slump floor into the Batagaika River (Fig. 1b). The high ice content of the exposed cryostratigraphic horizons (up to 87 % for the Upper IC; Table 1) ensures a deficit of solid sediments yield during thawing. The release of meltwater is sufficient to transport the relatively small volume of finely dispersed thawed mineral material. Additionally, snowmelt in spring as well as heavy rains and thunderstorms in summer provide substantial amounts of water for intensified sediment transport. The incision of the stream channel occurs as thermal erosion, when in some cases the incision is ahead of the thawing of sediments under the channel, and permafrost is exposed.

The main axial valley that cuts the thaw slump floor inherits the initial position of the ravine from which the Batagay thaw slump started forming (Kunitsky et al., 2013). In the central part of the thaw slump, the valleys of the minor confluents are parallel to each other and drain into the main valley almost at right angles (Fig. 10). Presumably, this distinct pattern of the erosion network was formed when the thaw slump was much smaller and more elongated along the initial ravine, and these valleys were consequently formed orthogonally to the receding walls of the thaw slump. Later on in the early 1990s, the thaw slump expanded, and the western and southwestern walls retreated more intensively (Savvinov et al., 2018). This is likely related to the upslope propagation of the thaw slump growth around this time that cut the ice-rich Upper IC whose near-surface distribution largely resembles the bowl-shape form of the upper thaw slump part. In contrast, the narrower lower part of the thaw slump is dominated by less ice-rich deposits of the Upper Sand near the surface (Table 1). The expansion of the thaw slump edges complicated and partly rebuilt the initial pattern of the erosion network and the present valley curvatures appeared.

Most erosion cuts have V-shaped or box-shaped valley transverse profiles with narrow ridges. The slopes of the ridges are mostly straight, on which there is a gradual shedding of fine sandy material during periods of thaw. The presence of a sufficient slope of the erosion network is an important condition to ensure material transport and the progressive growth of the thaw slump. The longitudinal profile of erosion ravines has a concave form, its inclination increases as it approaches the thaw slump headwalls (Fig. 11).

The cross-profile shape of thaw slump headwalls is determined by their cryolithological composition and insolation exposure. Steep slopes up to vertical walls and overhangs are observed along the western and southern headwalls where the Upper IC and Lower Sand are exposed. The parts of the wall which are built by the Lower Sand are vertical along its entire length (Fig. 4). The profiles of the Upper IC demonstrate a strong relationship with insolation exposure. In the northwestern part of the thaw slump, the Upper IC wall is steep (profiles 2 and 3, Fig. 6), and faces toward the south and southeast, the slope inclination decreases and the profile changes to a concave one (profiles 4–6; Fig. 6). We assume that this change in the Upper IC slope morphology is due to the fact that the western wall is characterized by the higher amount of incoming solar radiation seasonally and annually, which covers the entire height of the wall (Fig.7b). In this case, both the upper part of the wall, composed of the Upper IC, and the lower part of the wall, composed of the Lower Sand, retreat at similar rates, which ensures the overall vertical profile of the slope. The southwestern and southern walls are shaded in the middle of the day with maximum solar radiation, and the lower part of the wall, composed of the Lower Sand, is maximally shaded. Thus, the rates of thawing and retreat of this lower and relatively ice-poor part (Table 1, TVIC ca. 50–54 %) of the section are decreasing. The upper part of the section, composed of ice-rich Upper IC (Table 1, TVIC ca. 84–87 %), receives more solar radiation and deposits thaw due to diffuse radiation and warm air temperatures, resulting in a more intensive retreat. As a result, a two-part profile is formed that comprises a concave upper part (within the Upper IC) and a vertical lower part (within the Lower Sand).

On the northern and eastern walls of the thaw slump, the deposition of sandy material and diluvial washout predominate, as there are no areas with exposed ice-rich deposits.

Several sites with baydzherakhs are located at the floor of the thaw slump. The top height of the baydzherakh sites roughly corresponds to the base of the Upper IC. Consequently, baydzherakhs can either be the remaining central sedimentary parts of the ice-wedge polygons after the complete melt of ice wedges (residual stage according to Romanovsky,

Table 2
Statistics of morphometric characteristics of various types of relief areas within thaw slump floor. Relief type numbers in the left column correspond to the designations in Fig. 8c.

Relief type	Height [m a.s.l.]			Slope [degree]			Dissection [m]		
	Mean	Min	Max	Mean	Min	Max	Mean	Min	Max
A	235	195	288	36	0	88	8.3	1.4	16.0
B	235	197	282	28	0	89	5.9	2.4	13.2
C-1	252	231	285	26	0	87	4.9	2.3	9.8
C-2	250	255	268	26	0	85	4.9	2.4	9.9
C-3	248	235	270	21	0	89	3.5	2.2	7.3

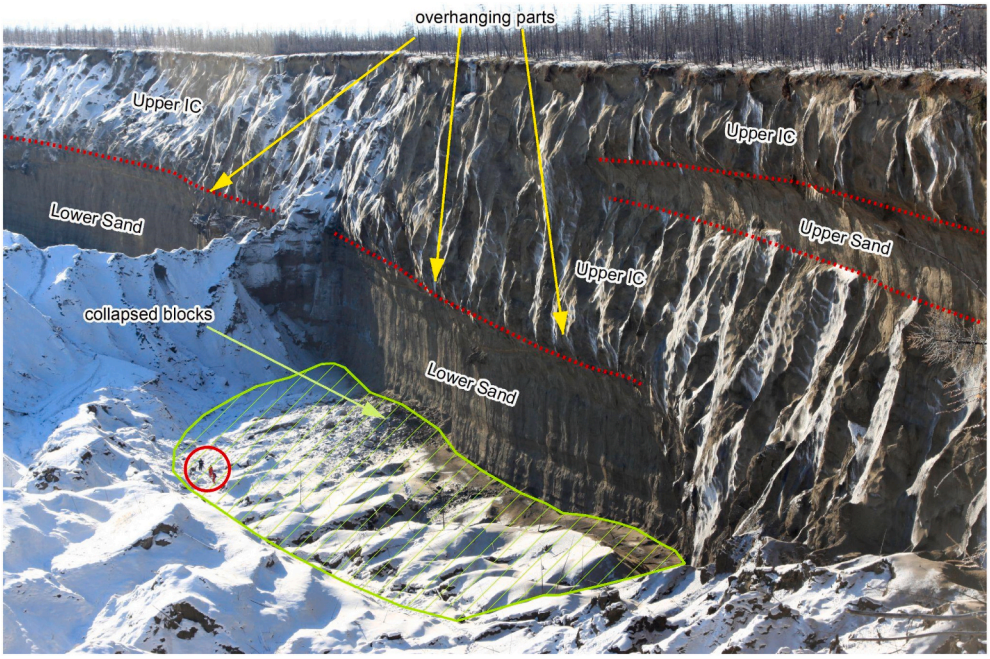

Fig. 9. Fragment of terrain with low dissection (C-3; marked in green) at the floor directly in front of the vertical retreating wall in the northwestern part of the thaw slump between sections I and II. Overhanging sediments of the Upper IC over a vertical wall of the Lower Sand are noted in the headwall and marked by yellow arrows. Cryolithological boundaries are marked as dotted red lines. Persons are circled in red for scale.

Fig. 10. Downslope view of the orthogonal pattern of minor confluents attached to the main valley that inherits the position of the initial thermal erosion ravine.

1977) or they represent a layer under which the lower parts of ice wedges are buried to a depth exceeding active layer thickness (conservation stage).

The western headwall with a maximum height and a steep vertical profile is built of exposed sediments of the Upper IC and the Lower Sand. Below these sections of the headwall, the slump floor is characterized by a flattened relief. Flattened areas at the floor of the thaw slump (C-3) are marked in two areas directly adjacent to the western wall. Presumably,

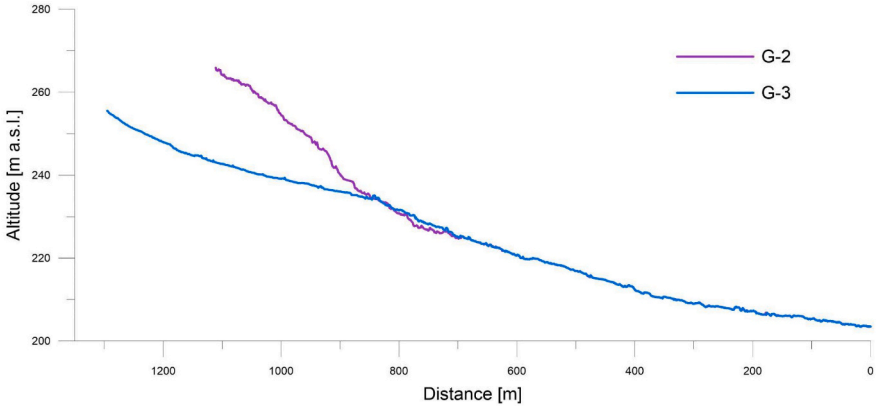

Fig. 11. Longitudinal profile along the two main erosion ravines (locations are indicated in Fig. 8c).

the formation of such surfaces is possible where ice content is locally increased in the section, which, during thaw, leads to a deficit of solid sediment yield and an excess amount of meltwater, which easily carries the collapsed and thawed material through the erosion network out of the thaw slump. For this part of the headwall, this effect is likely amplified by its exposure to insolation. Both effects facilitate the highest vertical headwall dimensions of the entire slump which in turn also leads to exposure of the lowermost stratigraphic unit (Lower Ice Complex) and the thickened Upper Ice Complex in the northern part, respectively.

The lowered heights of the flattened areas in the Batagay thaw slump floor, compared to the ridges within the main part of the floor, indicate that these flattened areas are a fairly new formation that did not exist earlier in the history of the thaw slump. If the appearance of such sites would be a common occurrence, they would be dissected by erosion and residual ridges as in the rest of the area. In this case, the heights of the residual ridges should approximately correspond, or rather, be slightly lower than these flattened areas. However, the opposite pattern is observed, flattened areas have lower heights. The observed deepening of the thaw slump floor below the western wall is likely associated with an increase in ice content in the part of the section that has been exposed and eroded in recent years. Probably, the sediments that built the central part of the thaw slump had somewhat lower ice contents.

Considering the above-mentioned assumption and the presence of baydzherakhs on the surface of a number of large remnants, we assume that these baydzherakhs mark areas where the lower parts of the ice wedges of the Upper IC melted only after the wall retreated. When the edge of the thaw slump was located in these areas, the height of the headwall was lower than the modern one and the foot of the wall did not reach the foot of the Upper IC. Accordingly, only the upper part of the section was affected by lateral thermal denudation. The lower parts of the ice wedges of the Upper IC melted out somewhat later, being situated on the gently sloping surface of the floor of the thaw slump. If so, thawing from above or frontal thermal denudation of the thermokarst type with subsidence of the surface above the melting ice wedges occurred, while the central sedimentary polygon centers remain somewhat longer and form the observed baydzherakhs. A similar situation can be observed in the course of profile 7 (Figs. 2, 6).

5. Discussion

5.1. Processes of thaw slump formation

Retrogressive thaw slumps occur exclusively in areas with high ground-ice content, such as tabular ground ice or the Yedoma Ice Complex (Runge et al., 2022). In terms of location, RTS can be situated on inland plains within slopes, where they occur when seasonal thawing affects ice-rich permafrost, and on retreating lake shores or river banks due to lateral erosion. A significant number of RTS are located on the Arctic sea coasts, undercut by thermal abrasion (Are, 1980).

The RTS shape in plan is either semicircular, bowl-shaped in cases when the landform starts to grow “from a point” with an initial mudflow from a local outcrop of ice-rich permafrost. RTS with an elongated shape along the coast, such as a thermal terrace, is formed, when the outcrop of ice-rich permafrost occurs along a wide front of a retreating coast of the sea or lake, i.e. “from a line”. Thus, the landform is determined by the local relief situation, the planar morphology and the thickness of the ice-rich horizon.

The large RTSs often are polycyclic forms and contain several cuts of different ages, sequentially embedded into each other (e.g., Lantuit et al., 2012). The stages of RTS active growth and expansion are followed by stabilization stages associated with the flattening of the RTS floor due to the accumulation of slumped material that exceeds seasonal thawing. In principle, this scheme is universal and is described in Lantuit and Pollard (2008) for the large onshore RTS on Herschel Island, as well as in Lantz and Kokelj (2008) for RTS of the Mackenzie Delta region and in Leibman et al. (2021) for RTS on the Yugorsky Peninsula. Unlike these large polycyclic RTS, there are no periods of stabilization of the Batagay thaw slump or a decrease in the activity of its expansion. From the end of the 1990s to present, there has been an ongoing retreat of the headwalls, increasing RTS area from year to year (Savvinov et al., 2018; Vadakkedath et al., 2020) although some slopes in the northern part of the headwall and in the lower part of the slump seems to have stabilized.

The set of relief-forming processes involved in RTS growth is fairly standard. Melting of ice-rich permafrost in the headwalls occurs as a result of the thermal effects of solar radiation and air heat. The ratio of meltwater to sediment in the thawed material is determined by total volumetric ice content. Meltwater flow promotes the formation of erosion cuts through which the thawed solid material is washed away. Some differences arise in the transportation of thawed and slumped material, depending on the location of the RTS close or at a distance from a lake or sea coast. The proximity of this base level of erosion and its constancy or mobility determines the shape of the longitudinal profile of erosional ravines.

The Batagay thaw slump is a unique permafrost degradation landform by its dimensions and the highest amounts of mobilized volumes ever reported. At coastal sections in the Laptev Sea region, steep headwalls of thaw slumps are commonly limited to and mainly built of Yedoma Ice Complex deposits reaching substantially lower heights such as up to about 15 m headwall height at both coasts of the Dmitry Laptev Strait on the southern shore of Bol'shoy Lyakhovsky Island (e.g., Wetterich et al., 2021) and the Oyogos Yar mainland coast (e.g., Tumskoy and Kuznetsova, 2022). The extraordinarily high headwalls of Batagay were formed due to both the presence of a very thick section of ice-rich Pleistocene deposits and its location on a slope which allows the removal of material due to erosion and the deepening of the thaw slump floor.

Similar significant heights of the retreating headwall, reaching up to 33 m, were recorded in one of the coastal thaw slumps on the Yugorsky Peninsula, where two horizons of tabular ground ice are exposed (Kizyakov, 2005). In the Canadian High Arctic on Ellesmere and Axel Heiberg islands, thaw slumps are observed in deposits containing massive ice bodies within marine deposits. Here, headwall heights are limited to about 20 m (Ward Jones et al., 2019) as also on Herschel Island in a similar setting in the Western Canadian Arctic (Lantuit and Pollard, 2008). Thaw slumps of the Peel Plateau formed in fluvially incised hummocky moraine deposits reach headwall heights of up to 33 m (Kokelj et al., 2017).

The combination of the aspect of the headwall with the exposed ice-rich horizons and the height of the outcrop determine the differences in the amount of incoming solar radiation. According to our field observations on the Yugorsky Peninsula (Kizyakov, 2005) as well as on Yamal Peninsula (Khomutov et al., 2017) and in the Canadian High Arctic (Ward Jones et al., 2019), RTSs located at high latitudes far north of the Arctic Circle, the headwall aspect (insolation exposure) during the polar day is not as important as for more southern RTS such as the Batagay thaw slump. Here, we found a spatial links between the morphology of the headwalls and the floor terrain, and the peculiarity of the cryolithological structures of the exposed strata (mainly the total volumetric ground ice content) as well as with the insolation exposure of the headwalls.

5.2. *Expected future development of the Batagay thaw slump and the significance of rapid permafrost thaw*

The cryolithological structure of the headwall exposed during the survey in March–April 2019, the morphology of the slopes and the slump floor allow us to assume that further development and increase in the size of the thaw slump is very likely in coming years. The highest growth rates are expected on the western and southern headwalls. The northwestern part of the edge may stop retreating, as in this area the ice content is low and the thaw slump is expected to merge with the ravine north of the slump that has stabilized slopes (partly seen in Figs. 1b and 2). Further, we assume that the walls built of ice-poor Upper Sand deposits in the northern and eastern parts will retreat at lower rates compared to those consisting of the ice-rich deposits of the Upper IC.

A potential limitation on growth of the thaw slump up the slope toward the southeast may be the reduction and complete disappearance of the ice-rich Upper IC when approaching the slopes of bedrock mountains such as Mount Khatyngnakh to the southwest, where bedrock almost reaches the surface and where crushed rock is mined in a quarry (Tumskoy et al., 2021), and also Mount Kirgillyakh to the northwest. Thus, the Batagay thaw slump might still grow in upcoming years and probably decades. However, as the presence of near-surface ice-rich deposits is the major precondition for further development, the ice distribution will define the final dimensions of the growing thaw slump.

The emergence of thaw slumps can be due to both, natural causes and anthropogenic impacts. Forestry, clearing, transportation, exploration and mining activities on the Yana Upland since about the 1940s created small-scale thermo-erosional ravines at multiple sites – as it was the case for the Batagay thaw slump – which might easily develop into larger thaw slumps if ice-rich permafrost starts degrading (Savvinov et al., 2018). We assume that the erosional effect will be larger in the extensions of such thermo-erosional valleys that provide a routeway for rain and snowmelt than in other areas of the slump.

Savvinov et al. (2018) related episodes of extraordinary warm and/or wet summers in past decades to intensified thermal denudation in the Batagay thaw slump, emphasizing the climate sensitivity of large-scale and rapid permafrost disturbance. Runge et al. (2022) assessed the distribution of retrogressive thaw slumps and their temporal dynamics across northern Siberia for 2001–2019, and revealed a >3-fold increase in area affected by retrogressive thaw slumps, intensified from 2016 onward. Such observations are in line with the projected intensification of abrupt permafrost thaw (e.g., Nitzbon et al., 2020).

Taking into account anthropogenic global warming and its Arctic amplification, the activation of existing and the emergence of new thaw slumps is expected in those areas where intensified seasonal thawing has not yet affected deeper ice-rich sediments. The emergence of new thaw slumps is most likely in the northern regions of permafrost, where near-surface ice-rich sediments did not thaw during the Holocene optimum. Heatwaves and wildfires across Siberian tundra and taiga regions have become common every summer over the last decade (e.g. Kharuk et al., 2021), and have drastic consequences on ecosystems, but also on permafrost stability as they disturb the thermal balance required to maintain a stable frozen state (e.g., Yanagiya and Furuya, 2020).

Northern taiga landscapes with near-surface ice-rich permafrost such as Yedoma Ice Complex deposits are highly vulnerable to (thermal or mechanical) disturbance, and lose – if slightly disturbed – their bearing capacity to retain soil, leading to solifluction, mudflows and surface detachments; intensified by terrain gradients. This can be illustrated using a modern example close to the Batagay thaw slump. In summer 2018, about 2 km southeast of the Batagay thaw slump, a wildfire occurred (Fig. 12a). As observed 3 years later in September 2021, the post-fire succession of the vegetation cover took place by moss-lichen-grass communities including *Aulacomnium turgidum* (mountain groove-moss), *Cetraria cucullata* (lichen) and *Helictotrichon krylovii* (alpine oat-grass). In order to counteract the further spread of the wildfire in 2018, a firebreak, i.e. trench, was established that turned out to be a channel for temporary surface water and mud flow (Fig. 12b and c) in the following years. The absent (burnt) vegetation cover in 2019 (a significant area to the east of the thaw slump, shown in Fig. 1b) accompanied by increasing soil temperatures promoted initial surface subsidence and the activation of slope gullying. As a result of human fire-prevention measures and drainage in September 2021, erosion was activated in six gullies east of the Batagay thaw slump. The closest gully is 0.3 km from the outflow of the thaw slump. At a distance of 2 km from the thaw slump, there is a 4 km long gully with exposed wedge ice (Fig. 12d). Such initial permafrost degradation features might promote further thermal denudation and slump formation. However, one of the main concerns is the wildfire hazards in the region, in addition to warming and the vulnerability of the boreal ecosystem against these factors. From the anthropogenic point of view, firefighting measures should aim at preserving the forest, i.e. without disturbance of the soil and vegetation cover.

6. Conclusions

Using field data, aerial imagery, and a digital surface model obtained at the Batagay thaw slump, we were able to differentiate the internal structures of the thaw slump in detail into three terrain types on its floor and three headwall types. The floor terrain types are classified by height, slope and dissection within an orthogonal pattern of minor confluences connected to the main outflow channel that inherits the position of the initial thermal erosion ravine. The profile shapes of the headwall types are determined by the varying permafrost properties of the sections, including ice content and wedge-ice presence, and the varying diurnal and seasonal insolation of different parts of the headwall reaching up to 55 m below surface.

Flattened areas of the slump floor below the western wall caused by a higher ground ice content in this part of the section that is currently undergoing intense thermal denudation. The high total volumetric ice content values of the Upper Ice Complex (up to about 87 %) and in the Lower Sand (up to about 54 %) ensure high headwall retreat rates and a deficit of solid sediments that is easily washed out through the erosion network. At the present stage, thermal denudation on the headwalls is ahead of the transformation of the terrain of the thaw slump floor due to erosion.

Before the present state, the lower parts of the ice wedges did not melt in the laterally retreating vertical headwalls, but later as a result of permafrost thawing at the slump floor that resulted in the appearance of

Fig. 12. Local examples of the onset of permafrost degradation in the vicinity of the Batagay thaw slump as a result of wildfire impact and human fire prevention measures (see Fig. 1b for locations): (a) northern taiga site 2 km northeast of the Batagay thaw slump after wildfire in 2018, (b) and (c) anthropogenic firebreaks turned into a gully, and (d) exposure of wedge ice due to gully formation. Survey date: 2021-09-19.

(caption on next column)

baydzherakhs.

Even under the conditions of ongoing and intensified climate warming, it is likely that the expansion of the Batagay thaw slump will be spatially limited by the distribution of near surface ice-rich sediments up the hillslope. Although Batagay thaw slump initiation was not caused by climate warming, its further growth dynamics are believed to be amplified under current conditions with higher air and ground temperatures and more summer precipitation.

CRediT authorship contribution statement

AIK designed the study, conducted the UAV survey and permafrost sampling. Further, SW, TO, LLJ, JC, HM, AGS and IIS participated in the field work. AIK, SW and TO wrote the first draft of the paper. MVZ provided methodological support for UAV data processing. FG proposed ideas on peculiarities of the thaw slump terrain features and provided remote sensing data serving as reference. ANF and GG provided fieldwork support and funding. All co-authors contributed expertise and discussion to the final version of the paper.

Funding

AIK was supported by the Lomonosov Moscow State University research program "The cryosphere evolution under climate change and anthropogenic impact" (#121051100164-0). TO acknowledges funding by the Leverhulme Trust Research Project Grant RPG-2020-334. The MPI Yakutsk and AWI provided baseline funding for expedition logistics and sample processing.

Declaration of competing interest

The authors declare that they have no known competing financial interests or personal relationships that could have appeared to influence the work reported in this paper.

Data availability

Data will be made available on request.

Acknowledgements

We acknowledge Dmitry Ukhin for climbing and sampling in March/April 2019, and Ilya Kozhenikov, Stepan Vasiliev (Melnikov Permafrost Institute SB RAN Yakutsk) and the AWI Logistics Department for supporting field logistics. We are thankful to Lutz Schirrmeister, Justin Lindemann, Angélique Opitz, and Jonas Sernau (Sediment Laboratory, AWI Potsdam) for assisting with sample processing and lab work.

References

Are, F.E., 1980. Thermal Abrasion of Seashores. Nauka, Moscow (in Russian).

Are, F.E., 2012. Coastal Erosion of the Arctic Lowlands. Academic Publishing House Geo, Novosibirsk (in Russian).

Ashastina, K., Schirrmeister, L., Fuchs, M., Kienast, F., 2017. Palaeoclimate characteristics in interior Siberia of MIS 6–2: first insights from the Batagay permafrost mega-thaw slump in the Yana Highlands. Clim. Past 13, 795–818. https://doi.org/10.5194/cp-13-795-2017.

Ashastina, K., Kuzmina, S., Rudaya, N., Troeva, E., Schoch, W.H., Römermann, C., Reinecke, J., Otte, V., Savvinov, G., Wesche, K., Kienast, F., 2018. Woodlands and steppes: Pleistocene vegetation in Yakutia's most continental part recorded in the

Batagay permafrost sequence. Quat. Sci. Rev. 196, 38–61. https://doi.org/10.1016/j.quascirev.2018.07.032.
Barnes, E.A., Polvani, L.M., 2015. CMIP5 Projections of arctic amplification, of the North American/North Atlantic Circulation, and of their relationship. J. Clim. 28 (13), 5254–5271. https://doi.org/10.1175/JCLI-D-14-00589.1.
Bernhard, P., Zwieback, S., Hajnsek, I., 2022. Accelerated mobilization of organic carbon from retrogressive thaw slumps on the northern Taymyr Peninsula. Cryosphere 16, 2819–2835. https://doi.org/10.5194/tc-16-2819-2022.
Biskaborn, B.K., Smith, S.L., Noetzli, J., Matthes, H., Vieira, G., Streletskiy, D.A., Schoeneich, P., Romanovsky, V.E., Lewkowicz, A.G., Abramov, A., Allard, M., Boike, J., Cable, W.L., Christiansen, H.H., Delaloye, R., Diekmann, B., Drozdov, D., Etzelmüller, B., Grosse, G., Guglielmin, M., Ingeman-Nielsen, T., Isaksen, K., Ishikawa, M., Johansson, M., Johannsson, H., Joo, A., Kaverin, D., Kholodov, A., Konstantinov, P., Kröger, T., Lambiel, C., Lanckman, J.P., Luo, D., Malkova, G., Meiklejohn, I., Moskalenko, N., Oliva, M., Phillips, M., Ramos, M., Sannel, A.B.K., Sergeev, D., Seybold, C., Skryabin, P., Vasiliev, A., Wu, Q., Yoshikawa, K., Zheleznyak, M., Lantuit, H., 2019. Permafrost is warming at a global scale. Nat. Commun. 10 (1), 264. https://doi.org/10.1038/s41467-018-08240-4.
Brooker, A., Fraser, R.H., Olthof, I., Kokelj, S.V., Lacelle, D., 2014. Mapping the activity and evolution of retrogressive thaw slumps by tasselled cap trend analysis of a Landsat satellite image stack. Permafrost Periglac. Process. 25, 243–256. https://doi.org/10.1002/ppp.1819.
Burn, C.R., 2000. The thermal regime of a retrogressive thaw slump near Mayo,Yukon Territory. Can. J. Earth Sci. 37 (7), 967–981. https://doi.org/10.1139/e00-017.
Burn, C.R., Lewkowicz, A.G., 1990. Retrogressive thaw slumps. Can. Geogr. 34 (3), 273–276.
Cassidy, A.E., Christen, A., Henry, G.H.R., 2017. Impacts of active retrogressive thaw slumps on vegetation, soil, and net ecosystem exchange of carbon dioxide in the Canadian High Arctic. Arctic Sci. 3, 179–202. https://doi.org/10.1139/as-2016-0034.
Cohen, J., Screen, J., Furtado, J., Barlow, M., Whittleston, D., Coumou, D., Francis, J., Dethloff, K., Entekhabi, D., Overland, J., Jones, J., 2014. Recent Arctic amplification and extreme mid-latitude weather. Nat. Geosci. 7, 627–637. https://doi.org/10.1038/ngeo2234.
Costard, F., Gautier, E., Fedorov, A., Konstantinov, P., Dupeyrat, L., 2014. An Assessment of the Erosion Potential of the Fluvial Thermal Process during Ice Breakups of the Lena River (Siberia). Permafr. Periglac. Process. 25 (3), 162–171. https://doi.org/10.1002/ppp.1812.
Courtin, J., Perfumo, A., Andreev, A.A., Opel, T., Stoof-Leichsenring, K.R., Edwards, M. E., Murton, J.B., Herzschuh, U., 2022. Pleistocene glacial and interglacial ecosystems inferred from ancient DNA analyses of permafrost sediments from Batagay megaslump, East Siberia. Environ.DNA 00, 1–19. https://doi.org/10.1002/edn3.336.
French, H., Shur, Y., 2010. The principles of cryostratigraphy. Earth-Sci. Rev. 101, 190–206. https://doi.org/10.1016/j.earscirev.2010.04.002.
Fuchs, M., Nitze, I., Strauss, J., Günther, F., Wetterich, S., Kizyakov, A., Fritz, M., Opel, T., Grigoriev, M.N., Maximov, G.M., Grosse, G., 2020. Rapid fluvio-thermal erosion of a yedoma permafrost cliff in the Lena River Delta. Front. Earth Sci. 8, 336. https://doi.org/10.3389/feart.2020.00336.
Geocryological Map of the USSR, 1996. In: Yershov, E.D. (Ed.), Scale 1:2,500,000. State Cartographic Factory, Vinnytsia, Ukraine (in Russian).
Grechishchev, S.E., Shur, Y. (Eds.), 1990. Implementation of Composition and Structure of Frozen Ground in Prediction of Permafrost Related Geological Hazards - Manual. Ministry of Geology of USSR, Moscow (in Russian).
Grigorev, M.N., Kunitsky, V.V., Chzhan, R.V., Shepelev, V.V., 2009. On the change in geocryological, landscape and hydrological conditions in the Arctic zone of Eastern Siberia due to climate warming. Geogr. Nat. Resour. 2, 5–11 (in Russian).
Grigoriev, M.N., 2008. Cryomorphogenesis and Lithodynamics of Coastal Shelf Zone of the Seas of Eastern Siberia. Melnikov Permafrost Institute SB RAS, Yakutsk.
Grigoriev, M.N., 2019. Coastal retreat rates at the Laptev Sea key monitoring sites. PANGAEA (last access: 20 July 2022). https://doi.pangaea.de/10.1594/PANGAEA.905519.
Günther, F., Overduin, P.P., Sandakov, A.V., Grosse, G., Grigoriev, M.N., 2013. Short- and long-term thermo-erosion of ice-rich permafrost coasts in the Laptev Sea region. Biogeosciences 10, 4297–4318. https://doi.org/10.5194/bg-10-4297-2013.
Günther, F., Overduin, P.P., Yakshina, I.A., Opel, T., Baranskaya, A.V., Grigoriev, M.N., 2015a. Observing Muostakh disappear: permafrost thaw subsidence and erosion of a ground-ice-rich island in response to arctic summer warming and sea ice reduction. Cryosphere 9, 151–178. https://doi.org/10.5194/tc-9-151-2015.
Günther, F., Grosse, G., Wetterich, S., Jones, B.M., Kunitsky, V.V., Kienast, F., Schirrmeister, L., 2015. The Batagay mega thaw slump, Yana Uplands, Yakutia, Russia: permafrost thaw dynamics on decadal time scale. In: PAST Gateways - Palaeo-Arctic Spatial and Temporal Gateways - Third International Conference and Workshop. Terra Nostra 2015/1, pp. 45–46 (in Russian).
Harvey, A.H., 2014. Properties of ice and supercooled water. In: Haynes, W.M. (Ed.), Handbook of Chemistry and Physics, 95th edition. CRC Press, Boca Raton, FL, pp. 6–12.
IPCC, 2021. In: Masson-Delmotte, V., Zhai, P., Pirani, S.A., Connors, L., Péan, C., Berger, S., Caud, N., Chen, Y., Goldfarb, L., Gomis, M.I., et al. (Eds.), Climate Change 2021: The Physical Science Basis. Contribution of Working Group I to the Sixth Assessment Report of the Intergovernmental Panel on Climate Change. Cambridge University Press, Cambridge, UK.
Jongejans, L.L., Opel, T., Courtin, J., Meyer, H., Kizyakov, A.I., Syromyatnikov, I., Shepelev, A., Wetterich, S., 2021. In: Batagay Spring 2019. Reports on Polar and Marine Research, 749, pp. 155–210. https://doi.org/10.48433/BzPM_0749_2021.
Jongejans, L.L., Mangelsdorf, K., Karger, C., Opel, T., Wetterich, S., Courtin, J., Meyer, H., Kizyakov, A.I., Grosse, G., Shepelev, A.G., Syromyatnikov, I.I., Fedorov, A.N., Strauss, J., 2022. Molecular biomarkers in Batagay megaslump permafrost deposits reveal clear differences in organic matter preservation between glacial and interglacial periods. Cryosphere 16, 3601–3617. https://doi.org/10.5194/tc-16-3601-2022.
Kanevskiy, M., Shur, Y., Strauss, J., Jorgenson, T., Fortier, D., Stephani, E., Vasiliev, A., 2016. Patterns and rates of riverbank erosion involving ice-rich permafrost (yedoma) in northern Alaska. Geomorphology 253, 370–384. https://doi.org/10.1016/j.geomorph.2015.10.023.
Kharuk, V.I., Ponomarev, E.I., Ivanova, G.A., Dvinskaya, M.L., Coogan, S.C.P., Flannigan, M.D., 2021. Wildfires in the Siberian taiga. Ambio 50, 1953–1974. https://doi.org/10.1007/s13280-020-01490-x.
Khomutov, A., Leibman, M., Dvornikov, Y., Gubarkov, A., Mullanurov, D., Khairullin, R., 2017. Activation of cryogenic earth flows and formation of thermocirques on Central Yamal as a result of climate fluctuations. In: Mikoš, K., Vilímek, V., Yin, Y., Sassa, K. (Eds.), Advancing Culture of Living With Landslides. Springer, Cham, Switzerland, pp. 209–216. https://doi.org/10.1007/978-3-319-53483-1_24.
Kizyakov, A.I., 2005. Dynamics of thermal denudation processes on the coast of the Yugorsky Peninsula. Kriosf. Zemli (Earth Cryosphere) IX, 63–67 (in Russian).
Kizyakov, A.I., Zimin, M.V., Leibman, M.O., Pravikova, N.V., 2013. Monitoring of the rate of thermal denudation and thermal abrasion on the western coast of Kolguev Island, using high resolution satellite images. Kriosf. Zemli (Earth Cryosphere) XVII, 36–47 (in Russian).
Kokelj, S.V., Lantz, T.C., Kanigan, J., Smith, S.L., Coutts, R., 2009. Origin and polycyclic behaviour of tundra thaw slumps, Mackenzie Delta region, Northwest TerritoriesCanada. Permafr. Periglac. Process. 20, 173–184. https://doi.org/10.1002/ppp.642.
Kokelj, S.V., Tunnicliffe, J., Lacelle, D., Lantz, T.C., Chine, K.S., Fraser, R., 2015. Increased precipitation drives mega slump development and destabilization of ice-rich permafrost terrain, northwestern Canada. Glob. Planet. Chang. 129 (56–68), 2015. https://doi.org/10.1016/j.gloplacha.2015.02.008.
Kokelj, S.V., Lantz, T.C., Tunnicliffe, J., Segal, R., Lacelle, D., 2017. Climate-driven thaw of permafrost preserved glacial landscapes, northwestern Canada. Geology 45, 371–374. https://doi.org/10.1130/G38626.1.
Konishchev, V.N., 2009. Response of permafrost to the climate warming. Bulletin of Moscow State University, Series 5, Geography 4, 10–20 (in Russian).
Konishchev, V.N., Maslov, A.D., 1969. Physical causes of frontal growth of syngenetic polygonal ice wedges. Probl.Cryolithology 1, 24–33 (in Russian).
Koven, C.D., Ringeval, B., Friedlingstein, P., Ciais, P., Cadule, P., Khvorostyanov, D., Krinner, G., Tarnocai, C., 2011. Permafrost carbon-climate feedbacks accelerate global warming. Proc. Natl. Acad. Sci. U. S. A. 108 (36), 14769–14774. https://doi.org/10.1073/pnas.1103910108.
Kudryavtsev, V.A., Garagulya, L.S., Kondratieva, K.A., Romanovsky, N.N., Maksimova, L. N., Chizhov, A.B., 1979. Methods of Permafrost Survey. Publishing House of Moscow State University, Moscow (in Russian).
Kunitsky, V.V., Syromyatnikov, I., Schirrmeister, L., Skachov, Y.B., Grosse, G., Wetterich, S., Grigoriev, M.N., 2013. Ice-rich permafrost and thermal denudation in the Batagay area (Yana Upland, East Siberia). Kriosf. Zemli (Earth Cryosphere) XVI I (1), 56–58 (in Russian).
Lacelle, D., Brooker, A., Fraser, R.H., Kokelj, S.V., 2015. Distribution and growth of thaw slumps in the Richardson Mountains-Peel Plateau region, northwestern Canada. Geomorphology 235, 40–51. https://doi.org/10.1016/j.geomorph.2015.01.024.
Lachenbruch, A.H., 1962. Mechanics of thermal contraction cracks and ice-wedge polygons in permafrost. In: Geological Society of America Special Papers, vol.70. GSA, Boulder.
Lantuit, H., Pollard, W.H., 2005. Temporal stereophotogrammetric analysis of retrogressive thaw slumps on Herschel Island, Yukon Territory. Nat. Hazards Earth Sys. Sci. 5, 413–423. https://doi.org/10.5194/nhess-5-413-2005.
Lantuit, H., Pollard, W.H., 2008. Fifty years of coastal erosion and retrogressive thaw slump activity on Herschel Island, southern Beaufort Sea, Yukon Territory, Canada. Geomorphology 95, 84–102. https://doi.org/10.1016/j.geomorph.2006.07.040.
Lantuit, H., Pollard, W.H., Couture, N., Fritz, M., Schirrmeister, L., Meyer, H., Hubberten, H.-W., 2012. Modern and late Holocene retrogressive thaw slump activity on the Yukon Coastal Plain and Herschel Island, Yukon TerritoryCanada. Permafr. Periglac. Process. 23, 39–51. https://doi.org/10.1002/ppp.1731.
Lantz, T.C., Kokelj, S.V., 2008. Increasing rates of retrogressive thaw slump activity in the Mackenzie Delta region, N.W.T., Canada. Geophys. Res. Lett. 35 (6), L06502 https://doi.org/10.1029/2007GL032433.
Leibman, M.O., Kizyakov, A.I., 2007. Cryogenic Landslides of Yamal and Yugorsky Peninsula. Earth Cryosphere Institute SB RAS, Moscow (in Russian).
Leibman, M.O., Gubarkov, A.A., Khomutov, A.V., Kizyakov, A.I., Vanshtein, B.G., 2008. Coastal processes at the tabular-ground-ice-bearing area, Yugorsky Peninsula, Russia. In: Proceedings of the 9th International Conference on Permafrost, 29 June – 3 July 2008, vol. 1. University of Alaska, Fairbanks, USA, Fairbarks, Alaska, pp. 1037–1042.
Leibman, M., Khomutov, A., Kizyakov, A., 2014. Cryogenic landslides in the West-Siberian Plain of Russia: classification, mechanisms, and landforms. In: Shan, W., Guo, Y., Wang, F., Marui, H., Strom, A. (Eds.), Landslides in Cold Regions in the Context of Climate Change. (Subseries: Environmental Science and Engineering). Springer, Cham, Switzerland, pp. 143–162. https://doi.org/10.1007/978-3-319-00867-7_11.
Leibman, M., Kizyakov, A., Zhdanova, Y., Sonyushkin, A., Zimin, M., 2021. Coastal retreat due to thermodenudation on the Yugorsky Peninsula, Russia during the last decade, update since 2001–2010. Remote Sens. 13 (20), 4042. https://doi.org/10.3390/rs13204042.

Maksimov, V.V., 1984. Estimates of the intensity of thermal denudation processes in the north of Yakutia. In: Study and Forecast of Cryogenic Physical-geological Processes. VSEGINGEO, Moscow, pp. 65–72 (in Russian).

Murton, J.B., Edwards, M.E., Lozhkin, A.V., Anderson, P.M., Savvinov, G.N., Bakulina, N., Bondarenko, O.V., Cherepanova, M.V., Danilov, P.P., Boeskorov, V., Goslar, T., Grigoriev, S., Gubin, S.V., Korzun, J.A., Lupachev, A.V., Tikhonov, A., Tsygankova, V.I., Vasilieva, G.V., Zanina, O.G., 2017. Preliminary paleoenvironmental analysis of permafrost deposits at Batagaika megaslump, Yana Uplands, northeast Siberia. Quat. Res. 87, 314–330. https://doi.org/10.1017/qua.2016.15.

Murton, J.B., Opel, T., Toms, P., Blinov, A., Fuchs, M., Wood, J., Gärtner, A., Merchel, S., Rugel, G., Savvinov, G., Wetterich, S., 2022. A multimethod dating study of ancient permafrost, Batagay megaslump, East Siberia. Quat. Res. 105, 1–22. https://doi.org/10.1017/qua.2021.27.

Nitzbon, J., Westermann, S., Langer, M., Martin, L.C., Strauss, J., Laboor, S., Boike, J., 2020. Fast response of cold ice-rich permafrost in northeast Siberia to a warming climate. Nat. Commun. 11, 220. https://doi.org/10.1038/s41467-020-15725-8.

Nitze, I., Grosse, G., Jones, B.M., Romanovsky, V.E., Boike, J., 2018. Remote sensing quantifies widespread abundance of permafrost region disturbances across the Arctic and Subarctic. Nat. Commun. 9, 5423. https://doi.org/10.1038/s41467-018-07663-3.

Nitze, I., Cooley, S.W., Duguay, C.R., Jones, B.M., Grosse, G., 2020. The catastrophic thermokarst lake drainage events of 2018 in northwestern Alaska: fast-forward into the future. The Cryosphere 14 (12), 4279–4297. https://doi.org/10.5194/tc-14-4279-2020.

Nitze, I., Heidler, K., Barth, S., Grosse, G., 2021. Developing and testing a deep learning approach for mapping retrogressive thaw slumps. Remote Sens. 13, 4294. https://doi.org/10.3390/rs13214294.

Opel, T., Murton, J.B., Wetterich, S., Meyer, H., Ashastina, K., Günther, F., Grotheer, H., Mollenhauer, G., Danilov, P.P., Boeskorov, V., Savvinov, G.N., Schirrmeister, L., 2019. Past climate and continentality inferred from ice wedges at Batagay megaslump in the Northern Hemisphere's most continental region, Yana Highlands, interior Yakutia. Clim. Past 15, 1443–1461. https://doi.org/10.5194/cp-15-1443-2019.

Overduin, P.P., Strzelecki, M.C., Grigoriev, M.N., Couture, N., Lantuit, H., St-Hilaire-Gravel, D., Günther, F., Wetterich, S., 2014. Coastal changes in the Arctic. In: Martini, I.P., Wanless, H.R. (Eds.), Sedimentary Coastal Zones From High to Low Latitudes: Similarities and Differences, Geological Society, London, Special Publications, 388, pp. 103–129. https://doi.org/10.1144/SP388.13 (in Russian).

Pizhankova, E.I., 2011. Thermodenudation in the coastal zone of the Lyakhovsky Island (interpretation of aerospace images). Kriosf. Zemli (Earth Cryosphere) XV (3), 61–70 (in Russian).

Pizhankova, E.I., Dobrynina, M.S., 2010. The dynamics of the Lyakhovsky Island coastline (results of aerospace image interpretation). Kriosf. Zemli (Earth Cryosphere) XIV (4), 66–79 (in Russian).

Romanovsky, N.N., 1977. Formation of Polygonal-Wedges Structures. Nauka, Novosibirsk (in Russian).

Romanovsky, V., Isaksen, K., Drozdov, D., Anisimov, O., Instanes, A., Leibman, M., McGuire, A.D., Shiklomanov, N., Smith, S., Walker, D., 2017. Chapter 4. Changing permafrost and its impacts. In: Arctic Monitoring and Assessment Programme (AMAP). Snow, Water, Ice and Permafrost in the Arctic (SWIPA); Summary for Policy-makers. Fairbanks, USA.

Runge, A., Nitze, I., Grosse, G., 2022. Remote sensing annual dynamics of rapid permafrost thaw disturbances with LandTrendr. Remote Sens. Environ. 268, 112752 https://doi.org/10.1016/j.rse.2021.112752.

Savvinov, G.N., Danilov, P.P., Petrov, A.A., Makarov, V.S., Boeskorov, V.S., Grigoriev, S. E., 2018. In: Environmental Problems of the Verkhoyansky Region, 6 (68). Vestnik of North-Eastern Federal University, pp. 18–33 (in Russian).

Schirrmeister, L., Froese, D., Tumskoy, V., Grosse, G., Wetterich, S., 2013. Permafrost and periglacial features | Yedoma: Late Pleistocene ice-rich syngenetic permafrost of Beringia. In: Elias, S.A., Mock, C.J. (Eds.), Encyclopedia of Quaternary Sciences, Second edition. Elsevier, Amsterdam, The Netherlands, pp. 542–552. https://doi.org/10.1016/b978-0-444-53643-3.00106-0.

Séjourné, A., Costarda, F., Fedorov, A., Gargani, J., Skorve, J., Massé, M., Mège, D., 2015. Evolution of the banks of thermokarst lakes in Central Yakutia (Central Siberia) due to retrogressive thaw slump activity controlled by insolation. Geomorphology 241, 31–40. https://doi.org/10.1016/j.geomorph.2015.03.033.

Shepelev, A.G., Kizyakov, A., Wetterich, S., Cherepanova, A., Fedorov, A., Syromyatnikov, I., Savvinov, G., 2020. Sub-surface carbon stocks in northern Taiga landscapes exposed in the Batagay megaslump, Yana Upland,Yakutia. Land 9, 305. https://doi.org/10.3390/land9090305.

Shestakova, A.A., Fedorov, A.N., Torgovkin, Y.I., Konstantinov, P.Y., Vasyliev, N.F., Kalinicheva, S.V., Samsonova, V.V., Hiyama, T., Iijima, Y., Park, H., Iwahana, G., Gorokhov, A.N., 2021. Mapping the main characteristics of permafrost on the basis of a permafrost-landscape map of Yakutia using GIS. Land 10, 462. https://doi.org/10.3390/land10050462.

Shur, Y., Hinkel, K.M., Nelson, F.E., 2005. The transient layer: implications for geocryology and climate-change science. Permafrost Periglac. Process. 16, 5–17. https://doi.org/10.1002/ppp.518.

Strauss, J., Laboor, S., Schirrmeister, L., Fedorov, A.N., Fortier, D., Froese, D., Fuchs, M., Günther, F., Grigoriev, M., Harden, J., Hugelius, G., Jongejans, L.L., Kanevskiy, M., Kholodov, A., Kunitsky, V., Kraev, G., Lozhkin, A., Rivkina, E., Shur, Y., Siegert, C., Spektor, V., Streletskaya, I., Ulrich, M., Vartanyan, S., Veremeeva, A., Anthony, K. W., Wetterich, S., Zimov, N., Grosse, G., 2021. Circum-arctic map of the Yedoma permafrost domain. Front. Earth Sci. 9, 758360 https://doi.org/10.3389/feart.2021.758360.

Streletskiy, D.A., Sherstiukov, A.B., Frauenfeld, O.W., Nelson, F.E., 2015. Changes in the 1963–2013 shallow ground thermal regime in Russian permafrost regions. Environ. Res. Lett. 10, 125005 https://doi.org/10.1088/1748-9326/10/12/125005.

Swanson, D.K., Nolan, M., 2018. Growth of retrogressive thaw slumps in the Noatak Valley, Alaska, 2010–2016, measured by airborne photogrammetry. Remote Sens. 10, 983. https://doi.org/10.3390/rs10070983.

Tsytovich, N.A., 1973. Mechanics of Frozen Soils (General and Applied). Publishing House High School, Moscow (in Russian).

Tumskoy, V., Kuznetsova, T., 2022. Cryolithostratigraphy of the Middle Pleistocene to Holocene Deposits in the Dmitry Laptev StraitNorthern Yakutia. Front. Earth Sci. 10, 789421 https://doi.org/10.3389/feart.2022.789421.

Tumskoy, V.E., Torgovkin, N.V., Romanis, T.V., 2021. Yakutian therocirques. In: Proceedings of the Annual Conference on the Results of Expedition Research: Relief and Quaternary Deposits of the Arctic, Subarctic and North-West Russia. Issue 8, St. Petersburg, Russia, pp. 252–257. https://doi.org/10.24412/2687-1092-2021-8-252-257 (in Russian).

Turetsky, M.R., Abbott, B.W., Jones, M.C., Walter Anthony, K., Olefeldt, D., Schuur, E.A. G., Grosse, G., Kuhry, P., Hugelius, G., Koven, C., Lawrence, D.M., Gibson, C., Sannel, A.B.K., McGuire, A.D., 2020. Carbon release through abrupt permafrost thaw. Nat. Geosci. 13, 138–143. https://doi.org/10.1038/s41561-019-0526-0.

Ulrich, M., Grosse, G., Strauss, J., Schirrmeister, L., 2014. Quantifying wedge-ice volumes in Yedoma and thermokarst basin deposits. Permafr.Periglac. Process. 25 (3), 151–161. https://doi.org/10.1002/ppp.1810.

Vadakkedath, V., Zawadzki, J., Przeździecki, K., 2020. Multisensory satellite observations of the expansion of the Batagaika crater and succession of vegetation in its interior from 1991 to 2018. Environ. Earth Sci. 79, 150. https://doi.org/10.1007/s12665-020-8895-7.

Van der Sluijs, J., Kokelj, S.V., Fraser, R.H., Tunnicliffe, J., Lacelle, D., 2018. Permafrost terrain dynamics and infrastructure impacts revealed by UAV photogrammetry and thermal imaging. Remote Sens. 10, 1734. https://doi.org/10.3390/rs10111734.

Vasil'chuk, Y.K., Vasil'chuk, J.Y., Budantseva, N.A., Vasil'chuk, A.C., Trishin, A.Y., 2019. High-resolution oxygen isotope and deuterium diagrams for ice wedges of the Batagai yedoma, Northern Central Yakutia. Doklady Earth Sci. 487, 975–978. https://doi.org/10.1134/S1028334X19080312 (in Russian).

Vasil'chuk, Yu.K., Vasil'chuk, J.Yu., Budantseva, N.A., Vasil'chuk, A.C., 2020. New AMS dates of organic microinclusions in ice wedges from the lower part of Batagay Yedoma, Yakutia. Doklady Earth Sci. 490, 100–103. https://doi.org/10.1134/S1028334X20020154.

Vasiliev, A.A., Gravis, A.G., Gubarkov, A.A., Drozdov, D.S., Malkova, G.V., Oblogov, G. E., Ponomareva, O.E., Sadurtdinov, M.R., Streletskaya, I.D., Streletskiy, D.A., Ustinova, E.V., Shirokov, R.S., Korostelev, Yu.V., 2020. Permafrost degradation: results of the long-term geocryological monitoring in the western sector of the Russian Arctic. Kriosf. Zemli (Earth Cryosphere) XXIV (2), 14–26 (in Russian).

Voskresensky, K.S., 2001. Modern Relief-forming Processes on the Plains of the North of Russia. Publishing House of the Faculty of Geography of Moscow State University, Moscow, Russia, 262 pp. (in Russian).

Ward Jones, M.K., Pollard, W.H., Jones, B.M., 2019. Rapid initialization of retrogressive thaw slumps in the Canadian high Arctic and their response to climate and terrain factors. Environ. Res. Lett. 14, 055006 https://doi.org/10.1088/1748-9326/ab12fd.

Wetterich, S., Meyer, H., Fritz, M., Mollenhauer, G., Rethemeyer, J., Kizyakov, A., Schirrmeister, L., Opel, T., 2021. Northeast Siberian permafrost ice-wedge stable isotopes depict pronounced Last Glacial Maximum winter cooling. Geophys. Res. Lett. 48, e2020GL092087 https://doi.org/10.1029/2020GL092087.

Yanagiya, K., Furuya, M., 2020. Post-wildfire surface deformation near Batagay, Eastern Siberia, detected by L-band and C-band InSAR. J. Geophys. Res. Earth Surf. 125, e2019JF005473 https://doi.org/10.1029/2019JF005473.

Zhigarev, L.A., 1975. Thermal Denudation Processes and Deformation Behavior of Thawing Sediments. Nauka, Moscow, Russia, 110 pp. (in Russian).